Madden–Julian Oscillation Impacts on Australian Temperatures and Extremes

ANDREW G. MARSHALL[a], MATTHEW C. WHEELER,[b] AND TIM COWAN[c,b]

[a] *Bureau of Meteorology, Hobart, Tasmania, Australia*
[b] *Bureau of Meteorology, Melbourne, Victoria, Australia*
[c] *Centre for Applied Climate Sciences, University of Southern Queensland, Toowoomba, Queensland, Australia*

(Manuscript received 31 May 2022, in final form 17 August 2022)

ABSTRACT: We assess seasonally varying impacts of the Madden–Julian oscillation (MJO) on Australian maximum and minimum temperature anomalies and extremes, and their modulation by El Niño–Southern Oscillation (ENSO), for the period June 1974–May 2022. Our composite-based approach uses observed temperatures from the Australian Gridded Climate Data, and 850-hPa wind data from the NCEP–NCAR reanalysis, to show how relationships to temperature and circulation evolve over the eight-phase life cycle of the MJO, which we derive from the real-time multivariate MJO index. The MJO has significant impacts on Australian temperatures and winds in all parts of the country at various times throughout the year, and to varying degrees. Two of the most pronounced impacts are 1) daytime warming across southeastern Australia in MJO phase 3 during spring associated with a strong anomalous anticyclone and 2) nighttime cooling over Queensland in MJO phase 7 during winter associated with anomalous advection of cool dry continental air. La Niña acts to significantly lessen both of these impacts, while El Niño enhances both the phase 3 warming over southern Australia in spring and the phase 7 overnight cooling over southern Queensland in winter. We show how the MJO can combine with El Niño and La Niña to have strong compounding influences, thus highlighting the importance of understanding interactions between multiple modes of climate variability and how they relate to Australian temperatures and extremes.

KEYWORDS: Australia; El Niño; La Niña; Madden-Julian oscillation; Extreme events; Climate variability

1. Introduction

There is a growing understanding of the importance of the Madden–Julian oscillation (MJO) (Madden and Julian 1971, 1972) for Australian agriculture (e.g., Donald et al. 2006; Wheeler et al. 2009; Marshall et al. 2014; Wang and Hendon 2020; Marshall et al. 2021; Cowan et al. 2022a). This understanding has been bolstered by recent examples of the MJO playing a key role in extreme weather and climate events in parts of northern and eastern Australia. For example, in late January and early February of 2019, the stalled convective component of an MJO event over the tropical western Pacific Ocean contributed to a devastating heavy rainfall, flooding, and an extreme cold episode over northeastern Australia that killed around 475 000 head of cattle and inundated over 3000 homes in the coastal Queensland city of Townsville (Cowan et al. 2019; Cowan et al. 2022a). Then in November of 2020, the suppressed phase of the MJO over the Maritime Continent played a key role in Australia's record heat[1] and severe lack of rainfall for the month despite an active La Niña event in the tropical Pacific Ocean (Lim et al. 2021). This had mixed impacts on cropping zones in New South Wales, with the dry November conditions helping the winter crop harvest in some areas but hindering the summer crop potential in others.[2]

The MJO is also a major driver of tropical cyclone (TC) variability on subseasonal time scales (e.g., Liebmann et al. 1994; Leroy and Wheeler 2008; Klotzbach 2014; Camp et al. 2018), having been shown to play an important role in TC genesis (e.g., Camargo et al. 2009) and track behavior (e.g., Ramsay et al. 2012). A recent example for Australia was TC Seroja, which formed in the Timor Sea during a strong MJO event in early April of 2021, resembling the Gill (1980) Rossby wave response to MJO convective heating on the equator (e.g., Yamagata and Hayashi 1984; Lau et al. 1989; Matthews 2000). As TC Seroja tracked southwest over the Indian Ocean, its chance interaction with another tropical system caused it to deviate toward the southwest Australian coast where it made landfall on 11 April.[3] The resulting damage to agricultural businesses and communities across the Western Australian Goldfields-Midlands and Midwest Gascoyne regions[4] showed how the MJO can remotely impact Australia's primary industries by influencing severe weather events downstream.

The MJO is known to affect subseasonal variations in Australia's climate via two distinct mechanisms: 1) as a direct response to its convective anomalies in the tropical north in all seasons except winter, and 2) indirectly resulting from remotely forced teleconnections that modulate the equatorial

[1] http://www.bom.gov.au/climate/current/month/aus/archive/202011.summary.shtml.

[2] https://www.dpi.nsw.gov.au/climate-landing/ssu/november-2020.

[3] http://www.bom.gov.au/cyclone/history/seroja.shtml.

[4] https://www.agric.wa.gov.au/news/announcements/tropical-cyclone-seroja-primary-industries-response.

Corresponding author: Andrew G. Marshall, andrew.marshall@bom.gov.au

DOI: 10.1175/JCLI-D-22-0413.1

trade winds in winter (when the MJO's convective component is shifted into the Northern Hemisphere) and the extratropical circulation year-round (e.g., Wheeler et al. 2009). While the focus of previous work has largely been on the MJO's modulation of Australian rainfall and circulation (e.g., Wheeler and Hendon 2004; Wheeler and McBride 2012; Donald et al. 2006; Wheeler et al. 2009), there is an emerging interest in the MJO's relationship to Australian temperature and extremes. Recent studies have demonstrated the role of the MJO on extreme heat across Australia during select phases of its life cycle in all seasons (Marshall et al. 2014), on overnight temperatures and extremes during the wintertime (Wang and Hendon 2020), on daytime temperatures and extremes during the spring (Marshall et al. 2022), and on both daytime and overnight temperatures during the northern Queensland floods of February 2019 (Cowan et al. 2022a). In this paper we provide the first comprehensive assessment for impacts of the MJO on Australian maximum and minimum temperatures and extremes in all seasons: austral summer [December–February (DJF)], autumn [March–May (MAM)], winter [June–August (JJA)], and spring [September–November (SON)]. We also explore the influence of El Niño–Southern Oscillation (ENSO), which is known to modulate MJO teleconnections to global climate (e.g., Hendon et al. 1999; Roundy et al. 2010; Moon et al. 2011; Ghelani et al. 2017; Son et al. 2017; Lee et al. 2019). Additionally, we assess wind anomalies at the 850-hPa level to provide a dynamical framework for understanding these teleconnections.

Descriptions of the analysis data and MJO index are provided in section 2. We assess the MJO's relationship to Australian maximum and minimum temperatures in section 3 and to temperature extremes in section 4. The modulation of these relationships by ENSO is presented in section 5, and we conclude with a summary of the key results in section 6.

2. Data and method

a. Madden–Julian oscillation index

The state of the MJO is depicted using the real-time multivariate MJO index pair, RMM1 and RMM2, from Wheeler and Hendon (2004). Calculated for each calendar day from 1 June 1974 to the present,[5] these indices capture the eastward-propagating large-scale structure of the MJO in zonal wind and convection along the equator, providing a measure of the strength and phase of the MJO. The RMM indices are the principal components of the leading pair of eigenvectors derived from a combined empirical orthogonal function analysis of equatorially averaged outgoing longwave radiation (OLR) and zonal wind at 200 and 850 hPa. Importantly, they are derived from data without the need for bandpass filtering and so can be used to assess the real time evolution of the MJO. RMM2 typically lags RMM1 by a quarter of a cycle, or about 10–15 days, and together they depict the eastward evolution of the MJO when plotted against one another in x and y coordinate space (Wheeler and Hendon 2004; Marshall et al. 2016). RMM1 and RMM2 may equivalently be expressed as a daily amplitude ($\sqrt{\text{RMM1}^2 + \text{RMM2}^2}$) and phase [$\tan^{-1}$(RMM2/RMM1)], which facilitates the construction of MJO composites in this study. We use the same eight phases as defined by Wheeler and Hendon (2004), with the MJO deemed to be in its active cycle when the RMM index amplitude is equal to or greater than one, and in a weak or inactive state when the RMM index amplitude is less than one. The MJO life cycle is depicted by active convection moving over the Indian Ocean in phases 2 and 3, over the Maritime Continent (directly north of Australia) in phases 4 and 5, and over the western and central Pacific Ocean in phases 6 and 7, with suppressed convection occurring a half cycle out of phase (e.g., over the Maritime Continent in phases 8 and 1). We use data spanning from 1 June 1974 to 31 May 2022 in this work to assess the MJO's impacts over a complete 48-yr dataset.

Another MJO index that has gained attention is recent years is the OLR MJO index (OMI; Kiladis et al. 2014), which was devised as an OLR-based univariate index for depicting the MJO when the convective signal is of primary interest. The OMI provides a useful assessment of composite MJO events (Kiladis et al. 2014) and can better discriminate the eastward and northward components of the MJO's propagation in austral winter compared to using the RMM indices (Kiladis et al. 2014; Wang et al. 2018). However, a disadvantage of using the OMI is its reliance on bandpass filtering, which cannot be done in real time, and thus its use for real time tracking is not straightforward (Kiladis et al. 2014; Wang et al. 2018). Our use of the RMM indices here is motivated by the application of this work to the Australian Bureau of Meteorology's operational real time MJO monitoring web pages at http://www.bom.gov.au/climate/mjo, which have recently been updated to feature the MJO teleconnection "averages" maps produced in this study and in our companion paper, Cowan et al. (2022b). The Wheeler and Hendon (2004) RMM indices are thus used consistently in all elements of this work.

b. El Niño–Southern Oscillation index

The state of ENSO is depicted using the Troup (1965) Southern Oscillation index (SOI) (e.g., McBride and Nicholls 1983), which is the standardized anomaly of the monthly mean sea level pressure (MSLP) difference between Tahiti (17°33′S, 149°37′E) and Darwin (12°26′S, 130°52′E).[6] Our choice of the SOI for this work over the ocean-based Niño indices follows Ghelani et al. (2017) and Cowan et al. (2022b), both of which use the SOI for assessing the combined impact of the MJO and ENSO on Australian rainfall given the reliability, and thus wide utility, of the SOI for supporting agricultural decision making in recent decades (Stone and Auliciems 1992; Stone et al. 1996). We source MSLP data from the Bureau of Meteorology, calculate a 3-month running mean SOI dataset for our seasonal analyses using the base period June 1974–May 2022, and define the phases of ENSO based

[5] http://www.bom.gov.au/climate/mjo/graphics/rmm.74toRealtime.txt.

[6] http://www.bom.gov.au/climate/enso/soi/about-soi.html.

on threshold SOI values of ±4. That is, values of the SOI lower than −4 are defined as El Niño, values greater than +4 are defined as La Niña, and values ranging between −4 and +4 are defined as ENSO neutral. Using a similar approach, Cowan et al. (2022b) tested the sensitivity of applying more restrictive threshold SOI values of ±8 (e.g., Ghelani et al. 2017) but found no deleterious effects on the combined ENSO–MJO signals.

c. Temperature and wind anomaly data

We explore the MJO's impact on maximum and minimum temperature across Australia using the Bureau of Meteorology's daily gridded AGCD (Australian Gridded Climate Data) version 1 (Evans et al. 2020). The AGCD combines available station observations for temperature with state-of-the-art statistical interpolation (e.g., Daley 1993; Glowacki et al. 2012) to provide high-resolution information on a 5-km horizontal grid. Brought into operation in September 2020, the AGCD replaces the Bureau of Meteorology's previous gridded temperature analysis, produced as part of the Australian Water Availability Project (Jones et al. 2009).

Zonal and meridional wind data at 850 hPa are from the daily National Centers for Environmental Prediction–National Center for Atmospheric Research (NCEP–NCAR) global reanalysis version 1 (Kalnay et al. 1996), available from 1948 to the present. We calculate anomalies relative to a daily climatology (using the full period to define the climatology) for both temperature and wind, and we assess significance at the 5% and 20% levels using Student's (1908) t test.

d. Temperature extremes

To assess the MJO's impact on Australian temperature extremes, we calculate the probability (frequency) of occurrence of daily maximum temperature anomalies above the 90th percentile (top decile) and daily minimum temperature anomalies below the 10th percentile (bottom decile) for each of the eight phases of the MJO when the MJO amplitude is greater than one. We define the percentiles for each season using the June 1974–May 2022 base period (not shown). Probability composites are computed by counting the number of instances at each grid location for which the maximum temperature anomalies fall within the top decile range, and for which the minimum temperature anomalies fall within the bottom decile range, and then dividing by the total number of samples in each composite. We display these as probability ratios calculated relative to the mean decile probability of occurrence (nominally 0.1; i.e., 1 in 10 defines the climatological occurrence of a decile event). Probability ratios greater than one indicate that an extreme event is more likely to occur than usual, and probability ratios less than one indicate a decreased likelihood of occurrence. For example, a probability ratio of 2 means the event is twice as likely to occur compared to normal, whereas a probability ratio of 0.5 means the event is half as likely to occur.

Significance is assessed using a z-score test for event probabilities (Spiegel 1961). The probabilities of occurrence of extremes in maximum and minimum temperature are assumed to be significantly different than the mean probability when the absolute value of z is greater than 1.96 (two-tailed distribution), and we account for the nonindependence of daily data samples N by computing the effective sample size N_{eff} [$\cong N(1-\rho)/(1+\rho)$], using the lag-1 autocorrelation ρ at each grid location.

3. MJO impact on maximum and minimum temperature anomalies

a. Maximum temperature

We begin by showing anomaly composites of daily maximum temperature and 850-hPa vector wind for each of the eight active MJO phases in DJF, MAM, JJA, and SON (Fig. 1). Composites are computed for each anomaly field by averaging over all days for which the MJO occurs in each phase. The number of days pertaining to each MJO phase composite is indicated at the bottom left of each figure panel. We note that the composite anomalies for the weak MJO phase are near zero across Australia, so we do not show these here; however, they may be viewed at http://www.bom.gov.au/climate/mjo. We also show the climatological seasonal means for maximum temperature and 850-hPa vector wind (Fig. 2, top row) and the standard deviation of daily maximum temperature anomalies (Fig. 2, bottom row).

The direct influence of the MJO's convective anomalies over northern Australia is strongly evident during summer (DJF; far left column of Fig. 1), with maximum temperature anomalies greater than 0.5°C occurring across broad northern areas in MJO phases 8, 1, 2, and 3 in concert with suppressed MJO convection and reduced rainfall (Wheeler et al. 2009; Cowan et al. 2022b). Conversely, significant daytime cooling occurs over parts of northern Australia in MJO phases 5, 6, and 7, with maximum temperature anomalies of less than −0.5°C (Fig. 1) corresponding to enhanced MJO convection and rainfall during those phases (Wheeler et al. 2009; Cowan et al. 2022b). Anomalous 850-hPa easterlies lag the warm signal, and anomalous 850-hPa westerlies lag the cool signal, by about one MJO phase (~1 week), consistent with the slight lag between the MJO's tropical zonal wind and rainfall anomalies (e.g., Hendon and Liebmann 1990; Wheeler et al. 2009). The direct influence of the MJO over northern Australia also extends into autumn (MAM; second column of Fig. 1), but the signal is noticeably weaker.

The MJO's remotely forced teleconnections to Australian climate are evident in all seasons. For summer, the strongest extratropical signals in maximum temperature occur in conjunction with meridional anomalies in the 850-hPa wind flow; in phase 4, northerly anomalies over southeastern Australia appear to drive a significant warming of up to 1.5°C in Tasmania and near the coasts of Victoria and southeast South Australia. Conversely, southerly anomalies occur in concert with cooler conditions over parts of southeastern Australia in phase 8. Since the mean 850-hPa winds in summer have a near-zero meridional component (Fig. 2), these meridional anomalies correspond to actual northerly and southerly flow. These signals are reflected in the very high daily standard deviation (more than 6°C) along

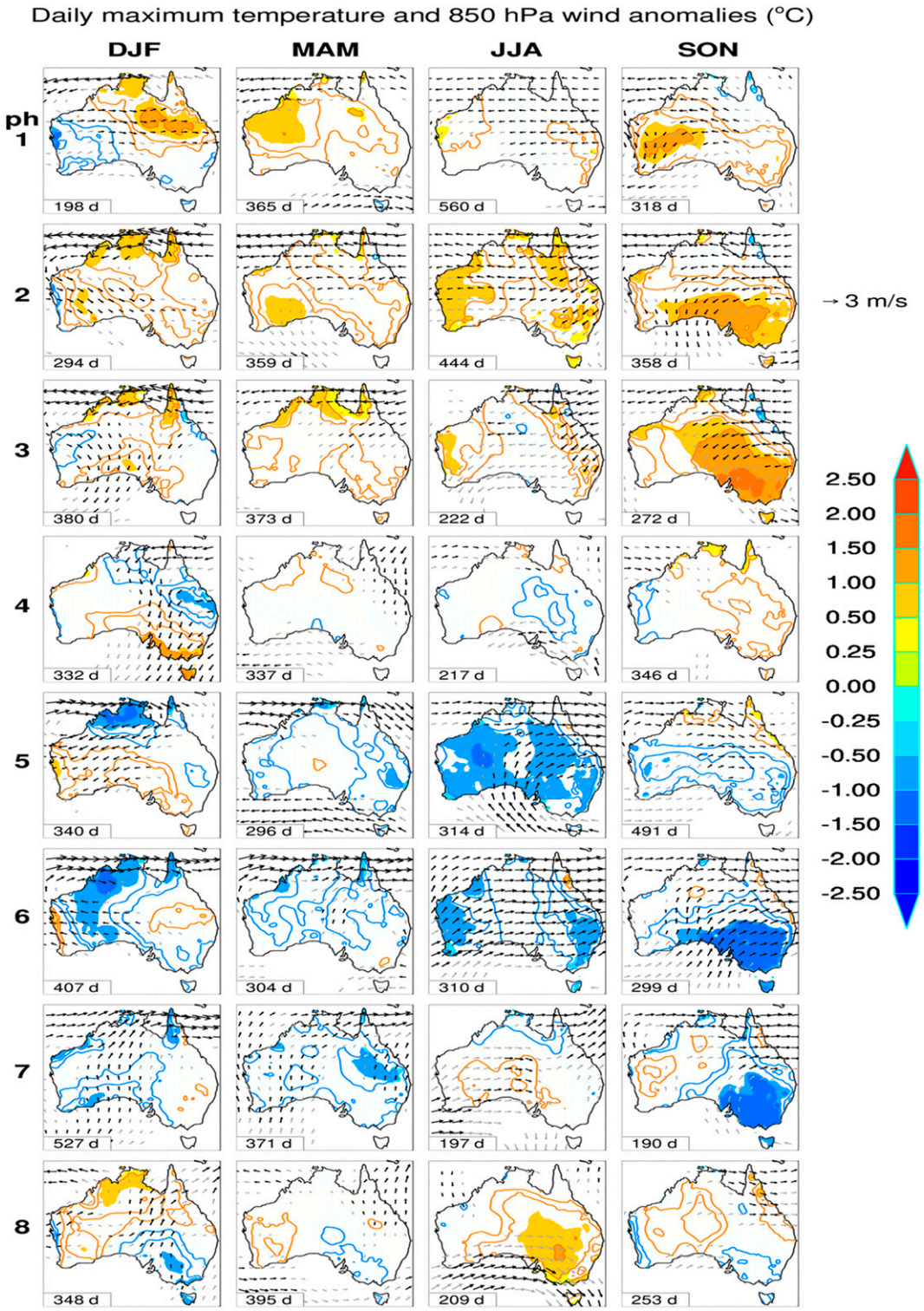

FIG. 1. Anomaly composites of daily maximum temperature (°C; contours and shading) and 850-hPa winds (m s^{-1}; vectors) in (first column) DJF, (second column) MAM, (third column) JJA, and (fourth column) SON, for each active MJO phase from 1 through 8 (shown from top to bottom). Shading is provided where the signal is statistically significant at the 5% level. For the winds, black vectors indicate significance at the 5% level, and gray vectors at the 20% level. The vector length for a wind speed of 3 m s^{-1} is indicated above the color bar for reference, and the number of days in each MJO phase is shown in the bottom left corner of each figure panel.

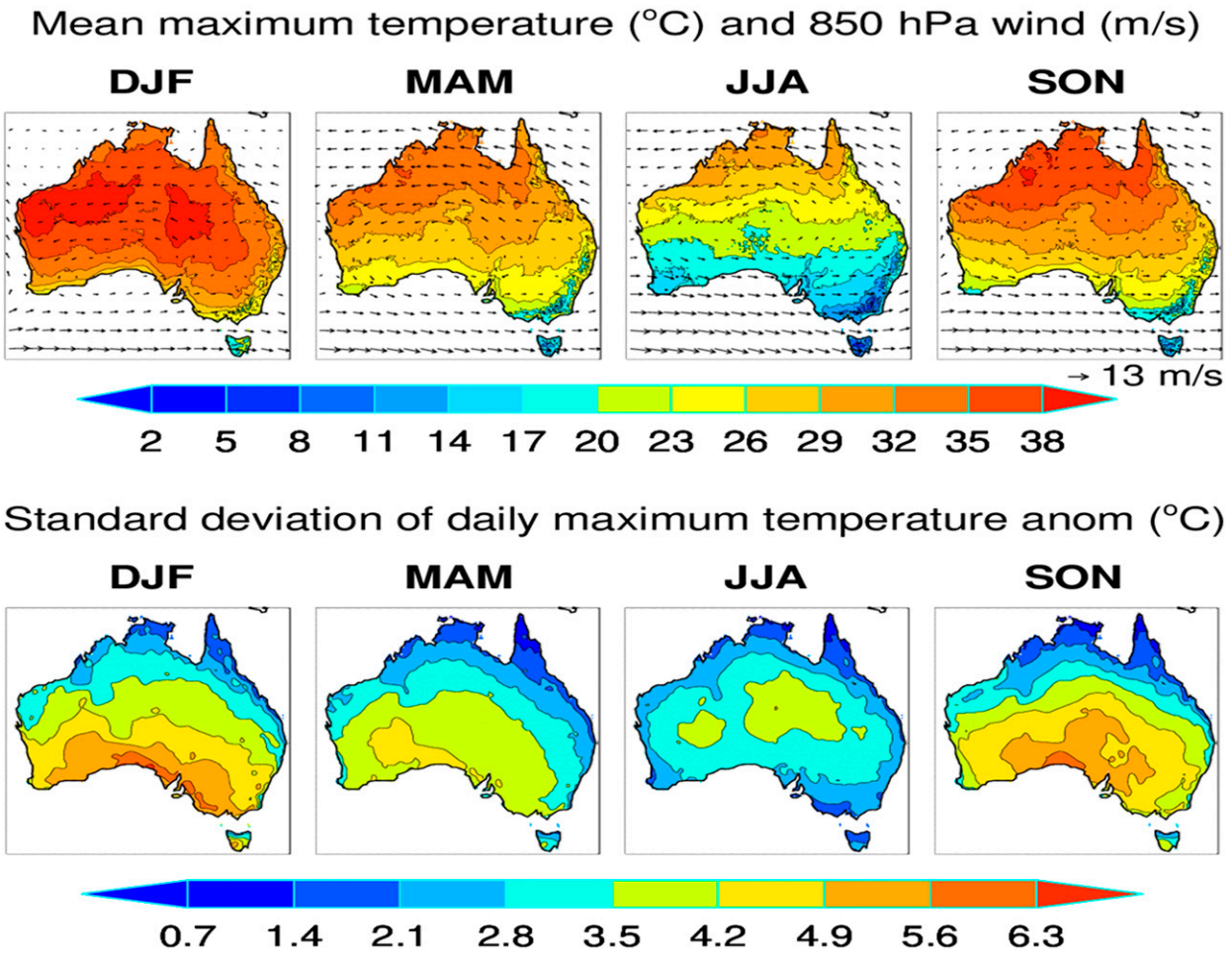

FIG. 2. (top) Climatological seasonal means for maximum temperature and 850-hPa vector wind and (bottom) standard deviation of daily maximum temperature anomalies in (first column) DJF, (second column) MAM, (third column) JJA, and (fourth column) SON. The vector length for the strongest mean wind speed, 13 m s^{-1}, is indicated below the top right panel for reference.

the South Australian and Victorian coastlines (Fig. 2). This points to a location that can be very hot in summer when a northerly wind blows from Australia's hot interior, and relatively cool when the wind blows from the south.

For autumn (MAM; second column of Fig. 1), the extratropical signals in maximum temperature are relatively weak but again indicate an association with meridional anomalies in the 850-hPa wind flow. Notably in phase 2, anticyclonic flow over the southern half of Australia appears to transport warmer air from central Australia to southern Western Australia where the mean maximum temperature increases by up to 1°C. This coincides with the location of the highest daily standard deviation (more than 4°C; Fig. 2). Conversely, southerly anomalies over the central (phase 6), western (phase 7), and eastern (phase 7) parts of extratropical Australia are seen in conjunction with a temperature reduction of comparable magnitude (most pronounced in phase 7 in southern central Queensland). We note that the autumn temperature anomalies in MJO phases 4 and 8 are near zero over northeastern Australia, despite the presence of northerly (phase 4) and southerly (phase 8) anomalous airflow. The expected warming influence of these northerly anomalies in phase 4 is likely to be offset by the influence of increased MJO rainfall at this time, which has a daytime radiative cooling effect (Wheeler et al. 2009; Cowan et al. 2022b). Conversely, the daytime radiative warming effect of drier conditions in MJO phase 8 would act to offset the cooling influence of southerly anomalies in this region.

Interestingly for winter (JJA; third column of Fig. 1) when the MJO's convection shifts into the Northern Hemisphere (e.g., Wang and Rui 1990), there appear strong influences from anomalies in the wind flow across the entire continent. These remote impacts can be understood as a combination of the strengthening/weakening of trade winds in the tropics and changes in the extratropical circulation (Wheeler et al. 2009). Over most of Australia, phases 1–3 are dominated by easterly anomalies and enhanced maximum temperature, while phases 5 and 6 are dominated by westerly anomalies and reduced

maximum temperature. In phases 1–3, significant warming of up to 1°C occurs over parts of Western Australia where the anomalous wind flows from Australia's warm interior (phases 1–3), and over parts of eastern Australia where the wind anomalies have a northerly component (phases 2 and 3). Conversely in phases 5 and 6, significant cooling of around 1°C occurs where the wind anomalies have a southerly component, associated with a Rossby wave train that propagates from the tropics into the Southern Hemisphere extratropics (Wang and Hendon 2020). Excited by enhanced MJO convection to the north of Australia in the Maritime Continent/western Pacific sector, this Rossby wave train emerges over Australia and propagates along a great circle route toward the south and east, extending over the Southern Ocean and impinging on South America (Wang and Hendon 2020). A pronounced warm signal of up to 1°C also occurs in phase 8 over southeastern Australia, in concert with a broad cyclonic (low pressure) anomaly that sits to the south of the continent. Anomalous westerlies extend over southern Australia in this case, suggesting the transport of relatively warm air from Australia's interior into the southeast.

Finally for spring (SON; far right column of Fig. 1), the maximum temperature composite signals again indicate primarily warmer conditions in phases 1–3 and cooler conditions in phases 5–7. However, unlike for the other seasons, the strongest springtime response to the MJO is a broad pattern of warming in phase 2 (up to 1.4°C) and phase 3 (up to 1.8°C) associated with strong anticyclonic flow, and cooling in phase 6 (down to −1.5°C) and phase 7 (down to −1.4°C) associated with strong cyclonic flow, over southern Australia. In phases 2 and 3, this occurs in conjunction with predominantly northeasterly flow from the anticyclonic (high pressure) anomaly, consistent with suppressed rainfall (Wheeler et al. 2009; Marshall et al. 2021) and an increased frequency of extreme heat (Marshall et al. 2014). Marshall et al. (2022) show that the heat signal in southwestern Australia is primarily driven by advection of warm air, while the signal in southeastern Australia is largely influenced by enhanced solar radiation at the surface. This occurs as part of a Rossby wave train that emanates from the Indian Ocean and disperses across the Southern Hemisphere in response to MJO convective heating on the equator (Marshall et al. 2022). The cooling in phases 6 and 7 occurs in conjunction with predominantly southerly flow from the cyclonic (low pressure) anomaly. (The latter signal is strongest in phase 6 when an associated increase in rainfall also occurs over parts of coastal Victoria, and over northern and eastern Tasmania; Wheeler et al. 2009; Cowan et al. 2022b.) The meridional components of these circulation anomalies correspond to actual northerly and southerly flow characteristics, which is again evident from the near-zero meridional component of the mean 850-hPa winds (Fig. 2). The strength and significance of the MJO's teleconnection to springtime temperature, circulation, and rainfall anomalies over southeastern Australia highlights the importance of the MJO for Australian agriculture at a time of year when productivity, such as crop yield and grain quality, can be highly sensitive to subseasonal variations in weather and climate (e.g., Nix 1987; Pook et al. 2006, 2009).

b. *Minimum temperature*

The MJO's impact on Australian minimum temperature was explored for the wintertime only in Wang and Hendon (2020). Here we expand on this previous work to provide a detailed assessment of the minimum temperature impacts for each MJO phase in DJF, MAM, JJA, and SON (Fig. 3). We note the year-round importance to agricultural communities of relationships to minimum temperature, considering the potential for warm summer nights to affect the ability of humans and livestock to cool themselves during a heatwave (e.g., Webb 2013), cold summer nights to produce devastating livestock chill conditions (e.g., Cowan et al. 2022a), and unseasonal temperatures during autumn and spring to affect crop production (e.g., Pook et al. 2006). We again show the climatological seasonal means for minimum temperature and 850-hPa vector wind (Fig. 4, top row), and the standard deviation of daily minimum temperature anomalies (Fig. 4, bottom row).

While the MJO's convective anomalies in austral summer have a strong and direct impact over northern Australia for maximum temperature (far left column of Fig. 1), they tend to have a more muted influence on minimum temperature (far left column of Fig. 3). A significant decrease (phase 1) and increase (phase 5) in minimum temperature of around 0.5°C occur over the Cape York Peninsula in concert with a decrease (phase 1) and increase (phase 5) in rainfall (Wheeler et al. 2009; Cowan et al. 2022b). This points to the role of suppressed MJO convection/increased OLR during phase 1, and increased MJO convection/reduced OLR during phase 5, for modulating the overnight longwave radiative heat loss in this region due to the associated changes in cloud cover. This influence is relatively weak, however, with the largest impacts on minimum temperature in summer occurring over parts of southern Australia in conjunction with the remotely forced anomalies in low level flow. Most notably, the MJO-induced northerly anomalies over Australia's southeast in phase 4 and southerly anomalies in phase 8 (see also Cowan et al. 2022b) appear to influence increases and decreases, respectively, in minimum temperature of up to 1.5°C. These coincide with the location of the highest daily standard deviation (Fig. 4). The fact that these warm and cool signals extend across a much larger spatial domain than those for maximum temperature (cf. Fig. 1) also suggests a key role for the MJO-induced high-level cloud/OLR anomalies that co-occur across much of this domain (Wheeler et al. 2009) in modulating overnight temperature. Significant increases in minimum temperature of up to 1°C also occur over parts of Western Australia's southern (phase 3) and westernmost (phases 5 and 6) regions, in conjunction with enhanced rainfall (Wheeler et al. 2009; Cowan et al. 2022b) and anomalous flow from the warm interior (Fig. 3).

For autumn (second column of Fig. 3), the influences on minimum temperature occur over broad areas of the country, particularly in MJO phases 4, 5, 7 and 8, in conjunction with anomalies in 850-hPa wind and rainfall (Wheeler et al. 2009; Cowan et al. 2022b). Large parts of Australia experience enhanced rainfall in phases 4 and 5, and phase 4 also produces

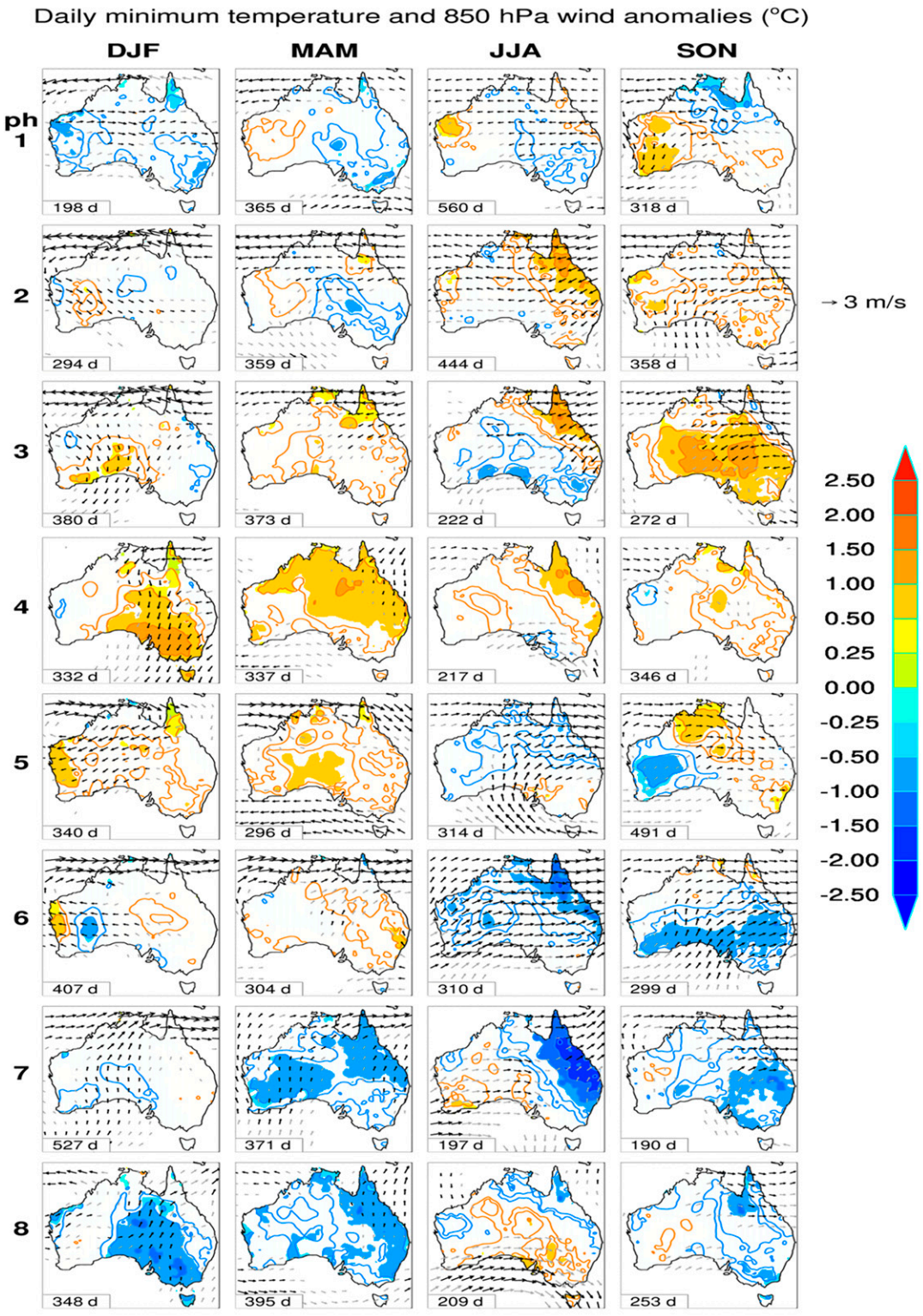

FIG. 3. As in Fig. 1, but for daily minimum temperature.

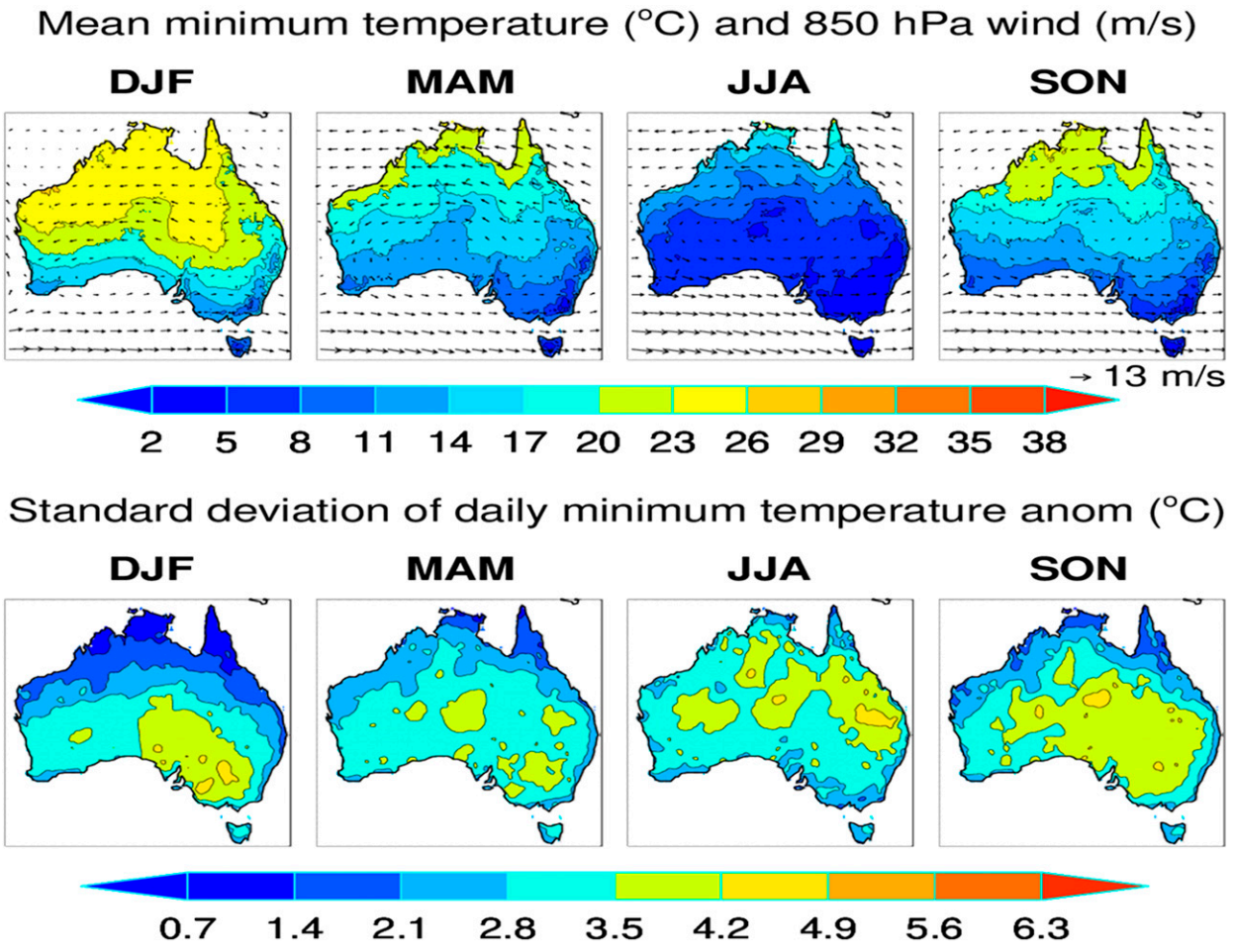

FIG. 4. As in Fig. 2, but for daily minimum temperature.

strong northerly anomalies over most of Queensland, both of which support warmer nights during these phases (Fig. 3) through reduced longwave radiative heat loss and an anomalous flow of warm air from the tropics (Wheeler et al. 2009; Cowan et al. 2022b). Warmer nights also occur over parts of eastern Australia in phase 6, in contrast to cooler days (cf. Fig. 1), but in the presence of weak wind anomalies. This points to the opposing radiative impacts of cloud cover on temperature during the day (reduced incoming solar radiation) compared with at night (reduced outgoing longwave radiation), associated with enhanced rainfall in phase 6 (Wheeler et al. 2009; Cowan et al. 2022b). Conversely, phases 7 and 8 are characterized by reduced rainfall (Wheeler et al. 2009; Cowan et al. 2022b), southerly wind anomalies, and thus cooler autumn nights over parts of the country (Fig. 3). These respective increases and decreases in minimum temperature are on the order of ±1°C.

The MJO's impacts on minimum temperature in winter (third column of Fig. 3) appear most pronounced over northeast Queensland in conjunction with strong rainfall and 850-hPa wind signals (Wheeler et al. 2009; Cowan et al. 2022b). Specifically, phases 2, 3, and 4 produce warmer winter nights when rainfall is enhanced in the presence of easterly/northeasterly anomalies. These easterly anomalies represent a strengthening of the trade winds in phases 2 and 3 and provide moist airflow from offshore in phase 4 (Wheeler et al. 2009). Weaker trades in phases 6 and 7 result from westerly/southwesterly anomalies that transport cool/dry continental air (Wang and Hendon 2020) and suppress rainfall along the northeast coast (Wheeler et al. 2009), leading to cooler winter nights. The respective increases and decreases in minimum temperature, which are on the order of 1.5°–2°C in some parts, influence the peak in standard deviation over southern Queensland (Fig. 4). The lack of any strong impact on maximum temperature over Queensland in phase 7 (cf. Fig. 1) is presumably due to compensating daytime warming from enhanced incoming shortwave radiation (Wang and Hendon 2020). Away from the northeast, increases in minimum temperature of up to 1.0°C complement the increases in maximum temperature (cf. Fig. 1) over parts of the far west during phases 1 and 2, and over southeastern Australia during phase 8, when the anomalous wind flows from Australia's warm interior.

Finally, for spring (far right column of Fig. 3), nighttime temperature responses to the MJO appear to be predominantly

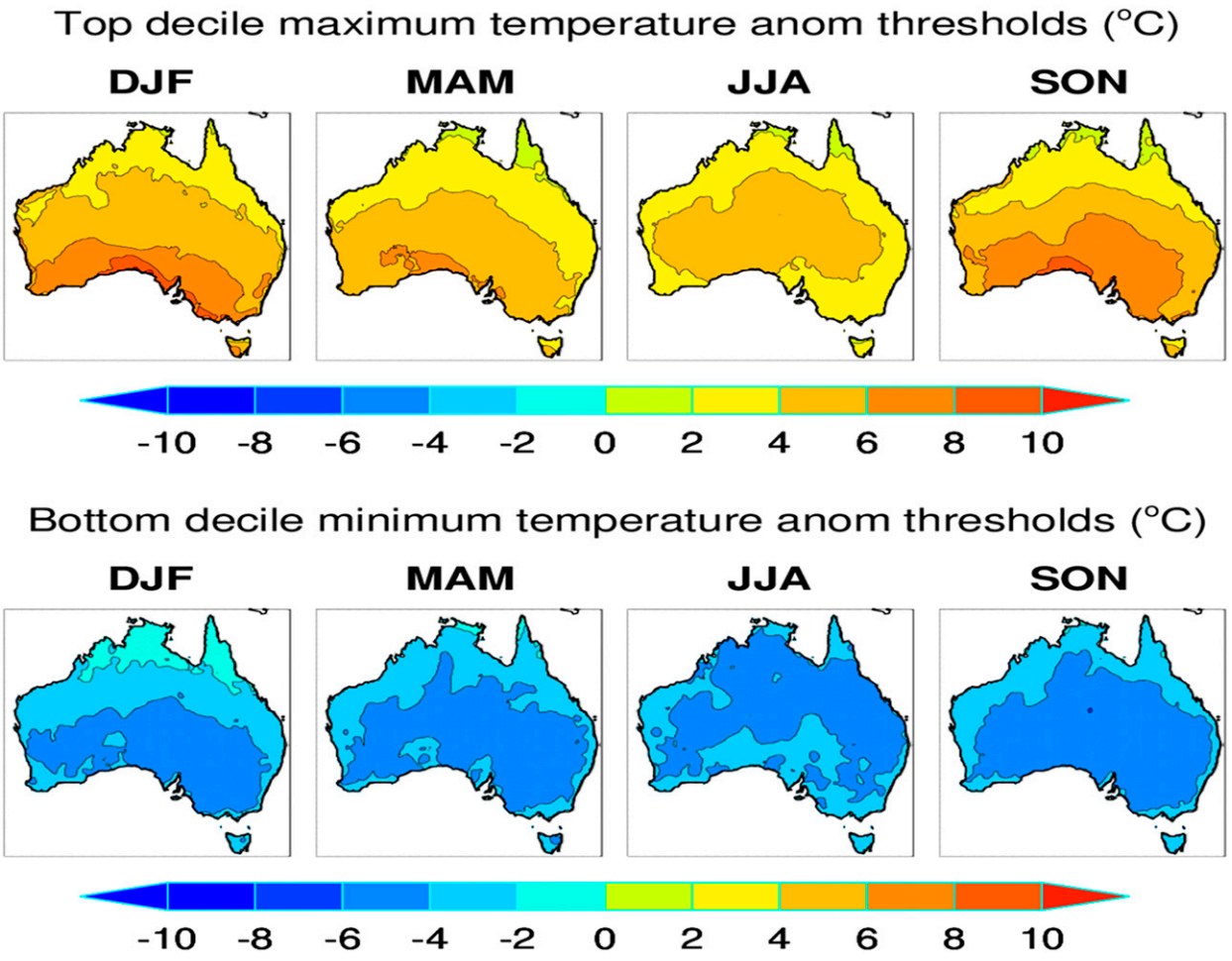

FIG. 5. Thresholds for (top) daily maximum temperature anomalies (Tmax; °C) above the 90th percentile and (bottom) daily minimum temperature anomalies (Tmin; °C) below the 10th percentile in (first column) DJF, (second column) MAM, (third column) JJA, and (fourth column) SON.

influenced by the broad-scale circulation anomalies, particularly in the extratropics. Over southeastern Australia, for example, MJO-induced rainfall is suppressed in phases 2 and 3 and enhanced in phase 6, yet despite the implications on changes in cloud cover and thus radiative heat loss/gain overnight, respective increases and decreases in minimum temperature of around 1.0°C or more occur in conjunction with strong northeasterly (anticyclonic; phases 2 and 3) and southwesterly (cyclonic; phase 6) anomalies. These translate to actual northerly and southerly flow characteristics, which respectively transport warmer air from lower latitudes and cooler air from higher latitudes. This influence is also apparent in the southeast during phase 7 (southerly anomalies and cooler nights) and in the southwest during phase 1 (northerlies and warmer nights). In the tropics, and in extratropical regions where the wind anomalies are relatively weak, the minimum temperature signal can be understood with regards to swings in rainfall. For example, cooler spring nights correspond to drier conditions (and thus clearer nights) over northern Australia in phase 1 and parts of central and eastern Australia in phase 8, while warmer nights correspond to wetter conditions (and thus cloudier nights) over parts of northern, central, and eastern Australia in phases 4 and 5 (Wheeler et al. 2009; Cowan et al. 2022b).

4. MJO impact on temperature extremes

a. Top decile maximum temperature

Marshall et al. (2014) introduced the role of the MJO in modulating the frequency of Australian extreme heat events for a small selection of cases. Here we update and expand upon that analysis by providing a full picture of the impacts for each MJO phase and season, based on the occurrence of daily maximum temperature anomalies exceeding the 90th percentile (i.e., top decile extreme events) at each grid location. The thresholds for exceedance are displayed in Fig. 5 (top row). Generally, the temperature anomaly thresholds increase from the tropics to the midlatitudes, except in winter when the highest threshold values occur inland over subtropical latitudes.

Anomaly threshold values range from around 1°–2°C in the northernmost regions year-round, to around 10°–11°C along parts of South Australia's coastline in spring and summer. This reflects the strong contrast between relatively low variability in daytime temperatures over the tropics, compared to high variability in the temperate midlatitudes during the warmer months (cf. standard deviation plots in Fig. 2).

Probability ratios for top decile daytime heat events are shown in Fig. 6 for each of the eight active MJO phases (rows) in each season (columns). We use bold contouring to indicate regions of statistical significance using a z-score test with effective sample sizes (described in section 2). Shaded regions indicate statistical significance using actual samples sizes for comparison; yellow-red shading represents an increase in the frequency of top decile events, and blue shading represents a decrease in frequency.

The MJO's relationship to extreme heat in Australia broadly resembles its impact on maximum temperature anomalies (cf. Fig. 1). The similarity between extreme and mean temperature responses has also been noted in previous work on other key drivers of Australian heat events (e.g., Alexander et al. 2009; Arblaster and Alexander 2012; Min et al. 2013). Notably, the likelihood of Australia's northernmost regions to experience a top decile heat event during summer increases in phases 8, 1, and 2, and decreases in phases 4–7, in direct response to the MJO's convective anomalies. The relationship in phase 3 is dominated by a strong signal over eastern Queensland that shows around half the normal likelihood of an extreme heat event. The fact that this signal appears significantly stronger than the phase 3 impact on average daytime temperature over eastern Queensland (cf. Fig. 1) suggests a greater MJO influence on the upper tail of the maximum temperature distribution than on the mean in this case. Southern Australia experiences up to twice the likelihood of an extreme heat event in phases 4 and 5 (mostly confined to Tasmania in phase 4), and around half the likelihood in phase 8 (mostly in the southeast), again consistent with the respective increases and decreases in mean maximum temperature, and associated northerly and southerly winds, induced by the MJO in summer.

For autumn and winter, parts of Australia again experience an increase in the likelihood of a top decile heat event (Fig. 6) over regions where the MJO influences warmer daytime conditions (cf. Fig. 1) in phases 8, 1, 2, and 3. Conversely, phases 5–7 show the largest decreases in event probability, particularly in winter when probability ratios of around 0.5 occur over parts of Australia's western (phases 5 and 6), southern (phase 6), northern (phase 7), and eastern (phases 6 and 7) regions. For southeastern Australia, the largest impacts again occur in the spring when extreme heat events are around twice as likely to occur than normal in phases 2 and 3, and half as likely in phases 6 and 7. These signals are most pronounced over southern Victoria and northwestern Tasmania in phase 3, and over much of the southeastern mainland and northern Tasmanian regions in phase 7, consistent with the Rossby wave train–driven warm northerly/anticyclonic and cool southerly/cyclonic influences at these times (Marshall et al. 2022).

b. *Bottom decile minimum temperature*

Here we compute the extremes analysis for bottom decile minimum temperature anomalies to assess the MJO's relationship to extremely cool nights over Australia. Figure 5 (bottom row) displays the 10th percentile thresholds of anomalous daily minimum temperature in each season. Threshold values range from around −1°C to around −6°C across the continent, with the strongest anomalies again dominating the southern Australian latitudes in all seasons except winter. We note that the range in these threshold values (~5°C) is considerably lower than the range in top decile maximum temperature values for spring and summer (~9°C). Thus, while daytime temperatures are highly variable over southern Australia during the warmer months, cool overnight temperatures are less variable and more spatially homogeneous (in an anomalous sense) across Australia, consistent with the standard deviation plots in Fig. 4.

Probability ratios for bottom decile minimum temperature are shown in Fig. 7 for each of the eight active MJO phases (rows) in each season (columns). For this analysis, blue shading represents an increase in event frequency and yellow-red shading represents a decrease in event frequency (in contrast to Fig. 6), such that an increased likelihood of extremely cool nights shares the same blue palette as negative overnight temperature anomalies in Fig. 3.

The MJO's relationship to cool nighttime extremes (Fig. 7) broadly resembles its impact on minimum temperature anomalies (Fig. 3). Large parts of the country experience a decrease in the likelihood of extremely cool nights at times when the MJO influences warmer nighttime conditions (mostly in phases 2–5), and an increase in the likelihood of extremely cool nights at times when the MJO influences cooler nighttime conditions (mostly in phases 6–8). For example, cool extremes are 2 or more times more likely to occur than normal over parts of eastern Australia in phase 8 during summer, parts of northern and western Australia in phases 7 and 8 during autumn, parts of northeastern Australia in phases 6 and 7 during winter, and parts of southern and eastern Australia in phases 6–8 during spring. The strongest of these signals is in phases 6 and 7 during winter when the frequency of cool extremes is more than doubled over northeast Queensland with the intrusion of cool/dry continental air (section 3b). Conversely, the frequency of wintertime cool extremes is reduced by more than two-thirds over northeast Queensland in phases 3 and 4 (Fig. 7) when the circulation anomalies are of opposite sign (i.e., influenced by moist onshore flow; Fig. 3). This is the combined result of radiative and advective nighttime cooling/warming from the MJO's tropical convection anomalies and an MJO-induced tropical–extratropical Rossby wave train over the Australian region in winter (Wang and Hendon 2020).

5. Modulation of MJO–temperature relationships by ENSO

The final part of this work explores the influence of ENSO on the MJO relationships to maximum and minimum temperature. We show how these relationships are modulated by El Niño in Fig. 8 (maximum temperature) and Fig. 9 (minimum

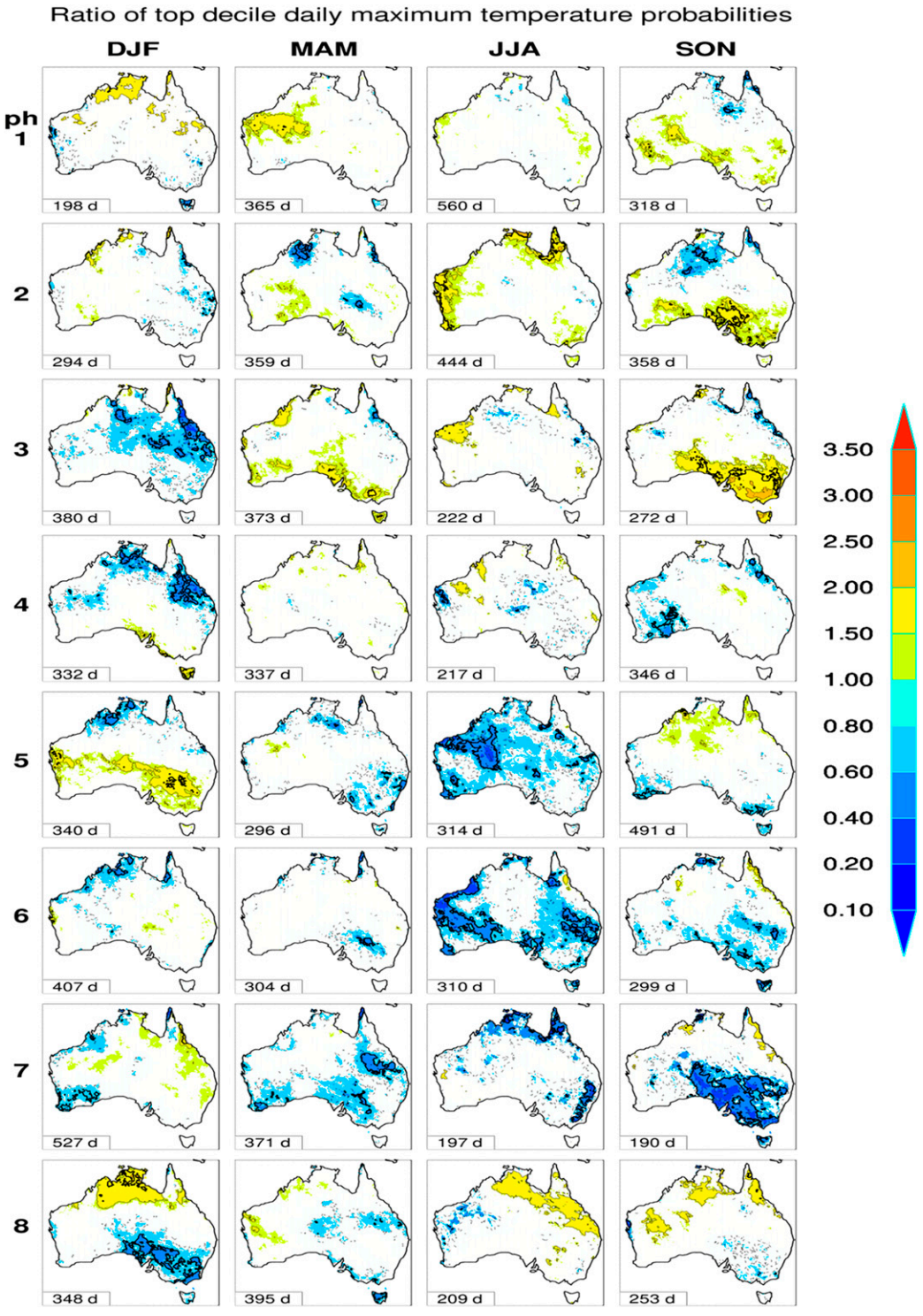

FIG. 6. Ratio of probabilities of top decile daily maximum temperature anomaly (Tmax) events in (first column) DJF, (second column) MAM, (third column) JJA, and (fourth column) SON, for each active MJO phase from 1 through 8 (shown from top to bottom). Ratios are calculated relative to the mean decile probability (nominally 0.1). Shaded regions indicate where the ratio is significantly different from one at 95% confidence using a z-score test for event probabilities with actual sample sizes. Bold contouring indicates a more stringent z-score test using effective sample sizes. Yellow-red shading represents an increase, and blue shading represents a decrease, in the frequency of top decile events. The number of days in each MJO phase is shown in the bottom-left corner of each figure panel.

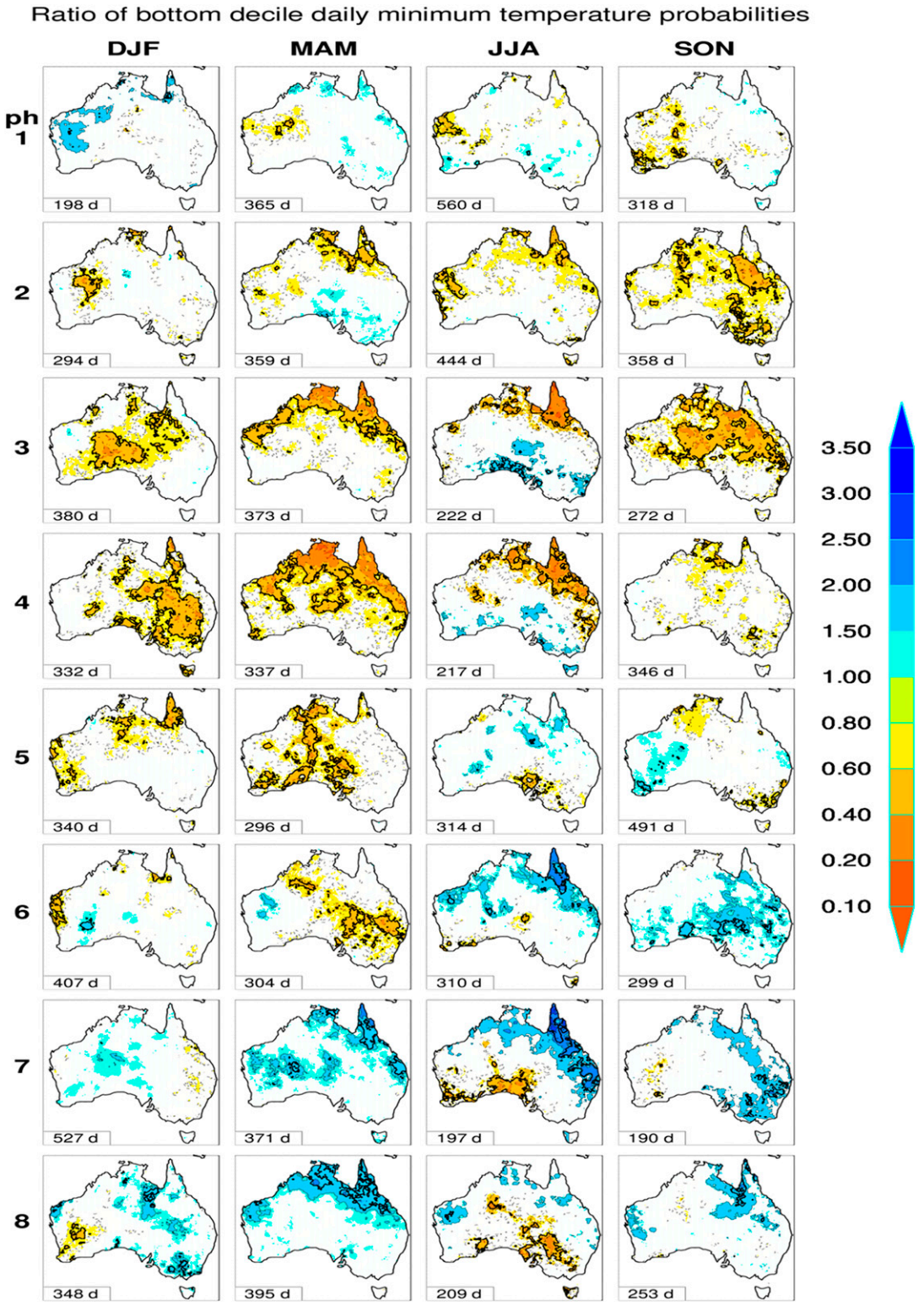

FIG. 7. As in Fig. 6, but for bottom decile daily minimum temperature anomalies (Tmin). Yellow–red shading represents a decrease, and blue shading represents an increase, in the frequency of bottom decile events.

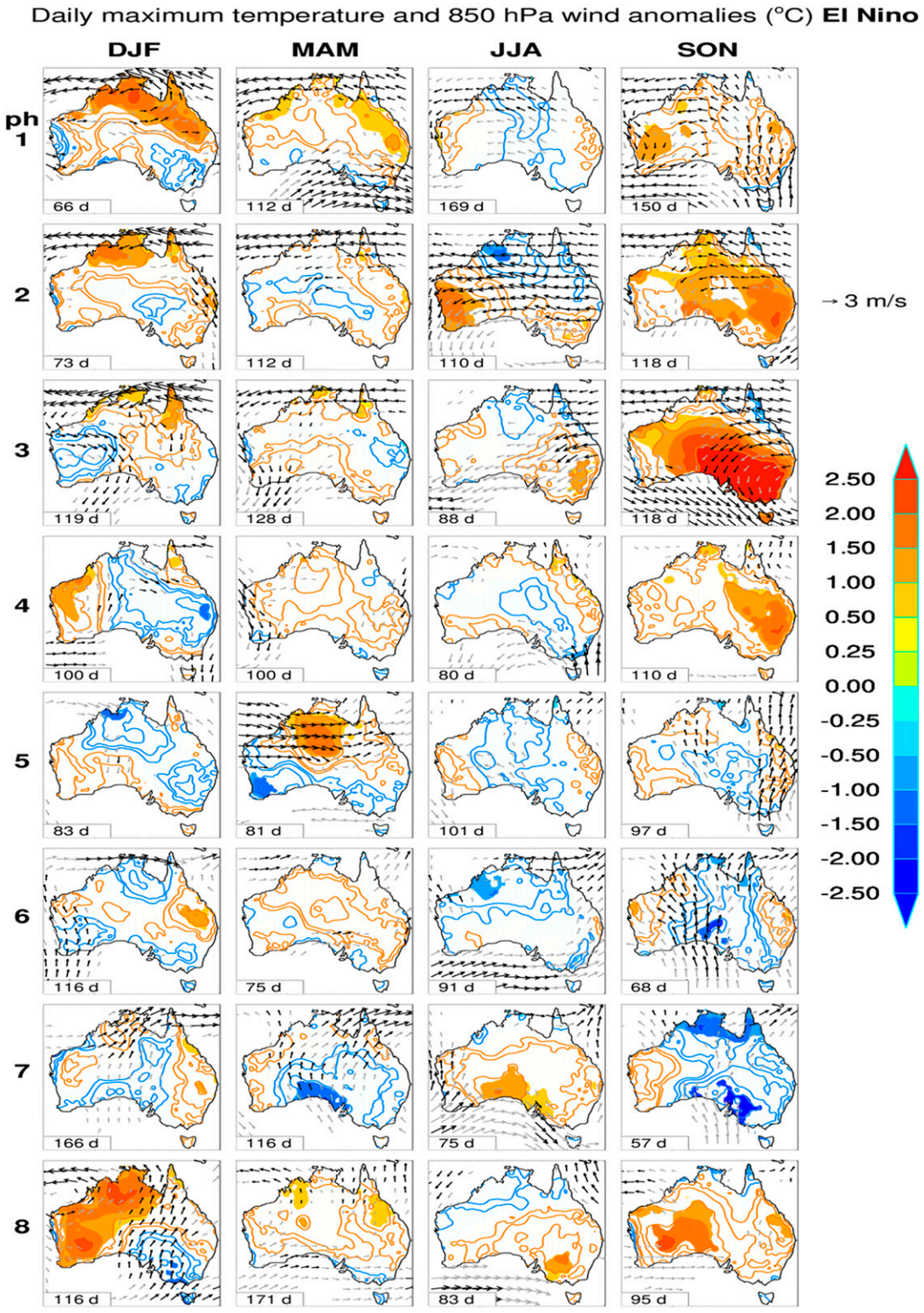

FIG. 8. As in Fig. 1, but for daily maximum temperature during El Niño years.

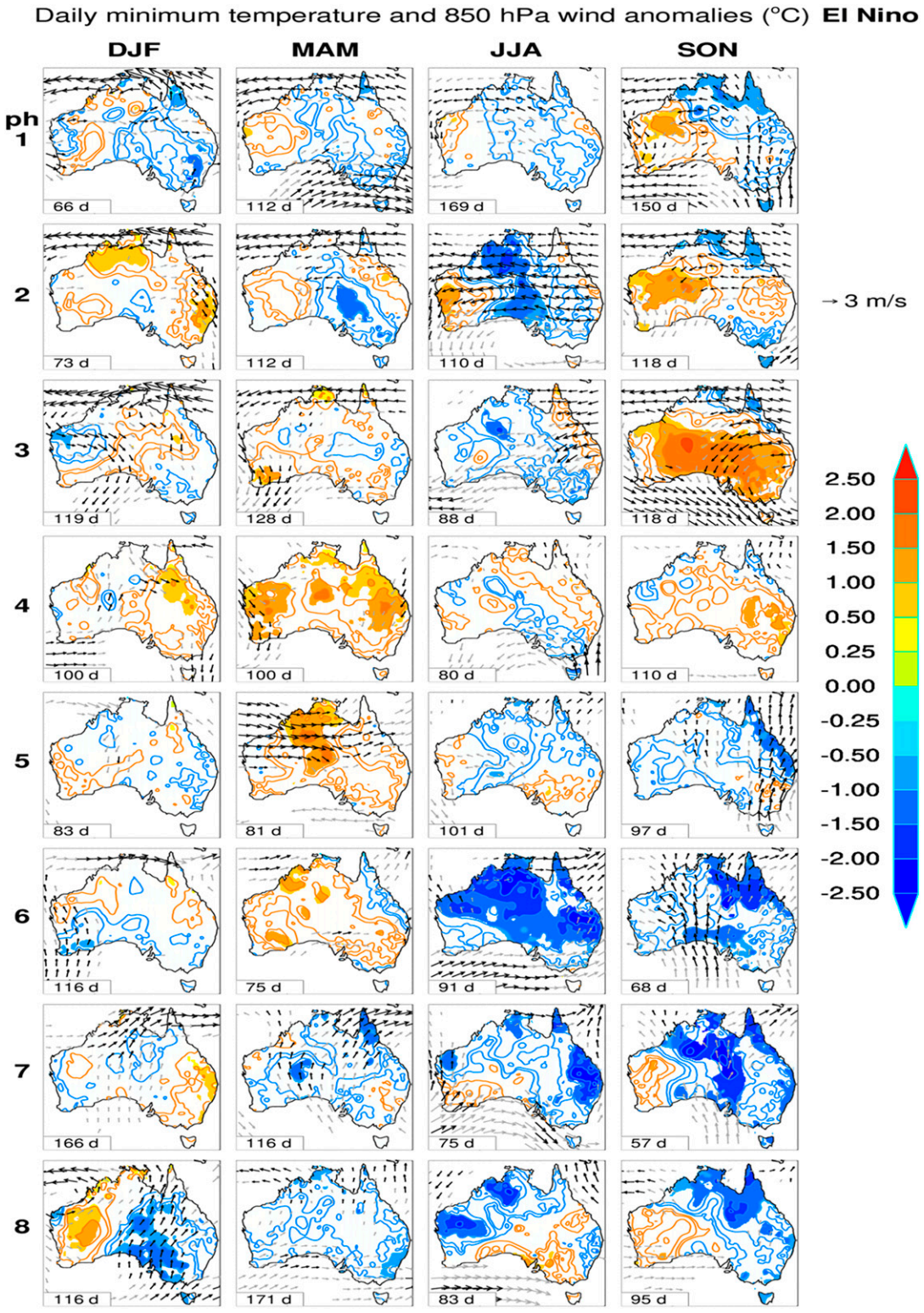

FIG. 9. As in Fig. 1, but for daily minimum temperature during El Niño years.

temperature), and by La Niña in Fig. 10 (maximum temperature) and Fig. 11 (minimum temperature), compared to neutral ENSO years in Fig. 12 (maximum temperature) and Fig. 13 (minimum temperature), in each season. In general, we see changes to the MJO–temperature signals that are consistent with the typical/average impacts of ENSO for Australia (Bureau of Meteorology 2022). However, there are some notable features that suggest a more complex dynamic between the MJO, ENSO, and Australian temperature, which we highlight here.

During an El Niño summer, daytime temperatures increase over Western Australia, Cape York, and the far southeast, and decrease elsewhere over the continent, in MJO phase 4 (far left column of Fig. 8). In the absence of strong wind forcing, these regions of warming and cooling occur in conjunction with respective decreases and increases in rainfall (Cowan et al. 2022b). Further, a concurrent increase in minimum temperature over eastern Australia (far left column of Fig. 9) suggests a reduction in overnight radiative heat loss associated with the rainfall increase (Cowan et al. 2022b).

During a La Niña summer, however, significant circulation anomalies appear to be the key driver of strong warming over southern Australia in MJO phase 4, for both maximum temperature (far left column of Fig. 10) and minimum temperature (far left column of Fig. 11). (The cooling elsewhere over Australia is consistent with the average temperature responses to La Niña; Bureau of Meteorology 2022.) Compared to neutral ENSO years (Figs. 12 and 13), La Niña events in MJO phase 4 during summer show an anomalous increase in northeasterly flow that transports warm continental air onto the southern coast, leading to an intensification and westward expansion of the coastal warming into South Australia, despite an increase in the probability of above median rainfall (and thus reduced shortwave daytime warming) over this region (Cowan et al. 2022b).

In MJO phase 8 during summer, the southerly oriented anomalies that flow across much of Australia in neutral ENSO years (Figs. 12 and 13) are considerably weaker over northern and western Australia during El Niño (Figs. 8 and 9) and absent over most of the continent during La Niña (Figs. 10 and 11). This likely influences stronger warming over northern and western Australia and weaker cooling over the southeast during El Niño, for both daytime (Fig. 8) and nighttime (Fig. 9) conditions. Compared to neutral ENSO years (Figs. 12 and 13), the southeastern cool signal in MJO phase 8 during summer is also weaker in La Niña years (Figs. 10 and 11) while the rest of Australia experiences cooler temperatures that are consistent with the average responses to La Niña (Bureau of Meteorology 2022) and that presumably relate to both reduced advection of warm continental air and enhanced rainfall at this time (Cowan et al. 2022b).

The influence of ENSO on the MJO–temperature signals in autumn varies considerably by MJO phase. In phase 1, cyclonic wind anomalies occur over southern Australia in conjunction with cooler daytime (second column of Fig. 8) and overnight (second column of Fig. 9) conditions during El Niño years (although the temperature anomalies are not statistically significant at the 5% level), whereas northerly anomalies over parts of northern-central Australia and northeasterly anomalies near the Great Australian Bight (significant at the 20% level) suggest an influence of warm airflow on anomalous increases in temperature over southern Australia during La Niña years (Figs. 10 and 11). ENSO alone has a weak relationship to autumn temperatures over most of Australia (Bureau of Meteorology 2022); however, when combined with MJO phase 5 we see a pronounced and widespread impact on maximum and minimum temperatures. During El Niño, daytime (Fig. 8) and overnight (Fig. 9) conditions warm by around 1°–2°C over much of central-northern Australia in conjunction with anomalous westerlies, while much of southern Australia experiences cooler days and warmer nights. During La Niña, most of Australia experiences strong and significant daytime cooling of around 1°–2°C in phase 5 (Fig. 10), and to a lesser degree overnight cooling (Fig. 11; significant only in Tasmania), except over parts of southwestern and northeastern Australia where overnight warming and modest daytime cooling occur in conjunction with anomalous advection of continental air into the southwest and tropical air into the northeast.

In winter, when the MJO tracks north of the equator, the combined ENSO–MJO impact on maximum and minimum temperature resembles the average impact of ENSO alone (Bureau of Meteorology 2022) in many regions. These include enhanced daytime warming in parts of southern Australia (third column of Fig. 8), overnight warming in parts of the southwest (third column of Fig. 9), and overnight cooling in parts of northern and eastern Australia, in most MJO phases during El Niño. Conversely, an average La Niña event in winter produces daytime cooling in parts of southern Australia (third column of Fig. 10), daytime warming in parts of the far north, overnight cooling in parts of the southwest (third column of Fig. 11), and overnight warming in parts of northern and eastern Australia, in most MJO phases. Notably for La Niña, its combined impact with the MJO is an anomalous reduction in southwesterly wind flow over northeastern Australia in phase 7, and thus less intense overnight cooling for Queensland (Fig. 11), compared to during El Niño (Fig. 9) and neutral ENSO years (third column of Fig. 13). About half an MJO cycle earlier (or later) in phase 2, the northeast experiences an increase in daytime temperature (Fig. 10) and overnight temperature (Fig. 11) of more than 1.5°C, in the presence of stronger anomalous wind flow from the north during La Niña.

Finally, for spring, MJO phase 3 during El Niño is a standout case that shows exacerbated daytime (far right column of Fig. 8) and nighttime (far right column of Fig. 9) warming associated with a strengthened anticyclone over southeastern Australia, compared to when all years are included in the analysis (Fig. 1). Comparison with the mean 850-hPa winds in Fig. 2 also suggests that these strong low-level circulation anomalies correspond to actual anticyclonic flow. The magnitude of peak daytime warming in phase 3 is 3.5°C during El Niño years (Fig. 8), which is at least two and a half times the peak warming during La Niña years (1.4°C; far right column of Fig. 10) and neutral ENSO years (1.2°C; far right column of Fig. 12), and thus El Niño itself appears to contribute to the strength of this teleconnection. Moreover, we saw earlier

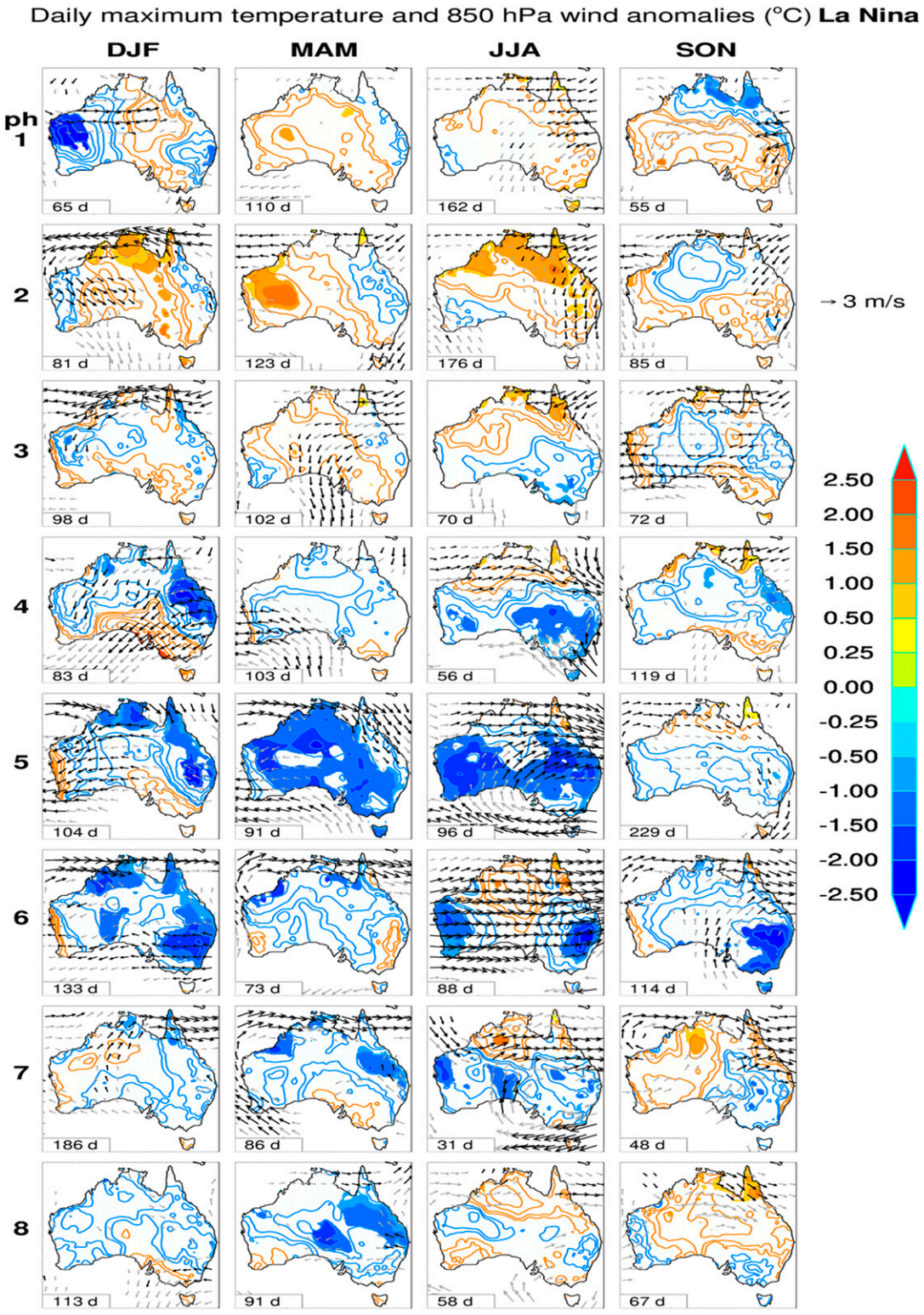

FIG. 10. As in Fig. 1, but for daily maximum temperature during La Niña years.

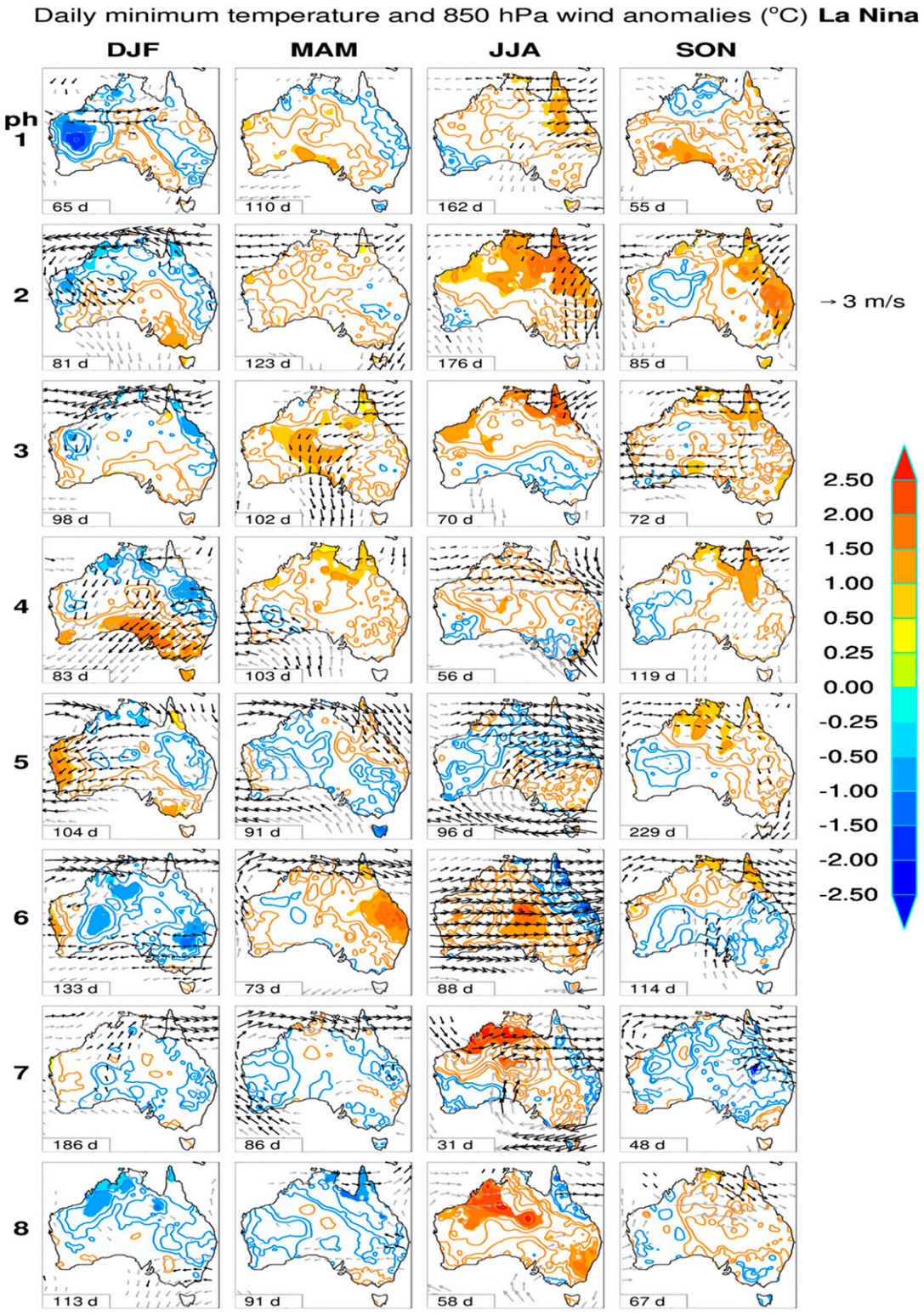

FIG. 11. As in Fig. 1, but for daily minimum temperature during La Niña years.

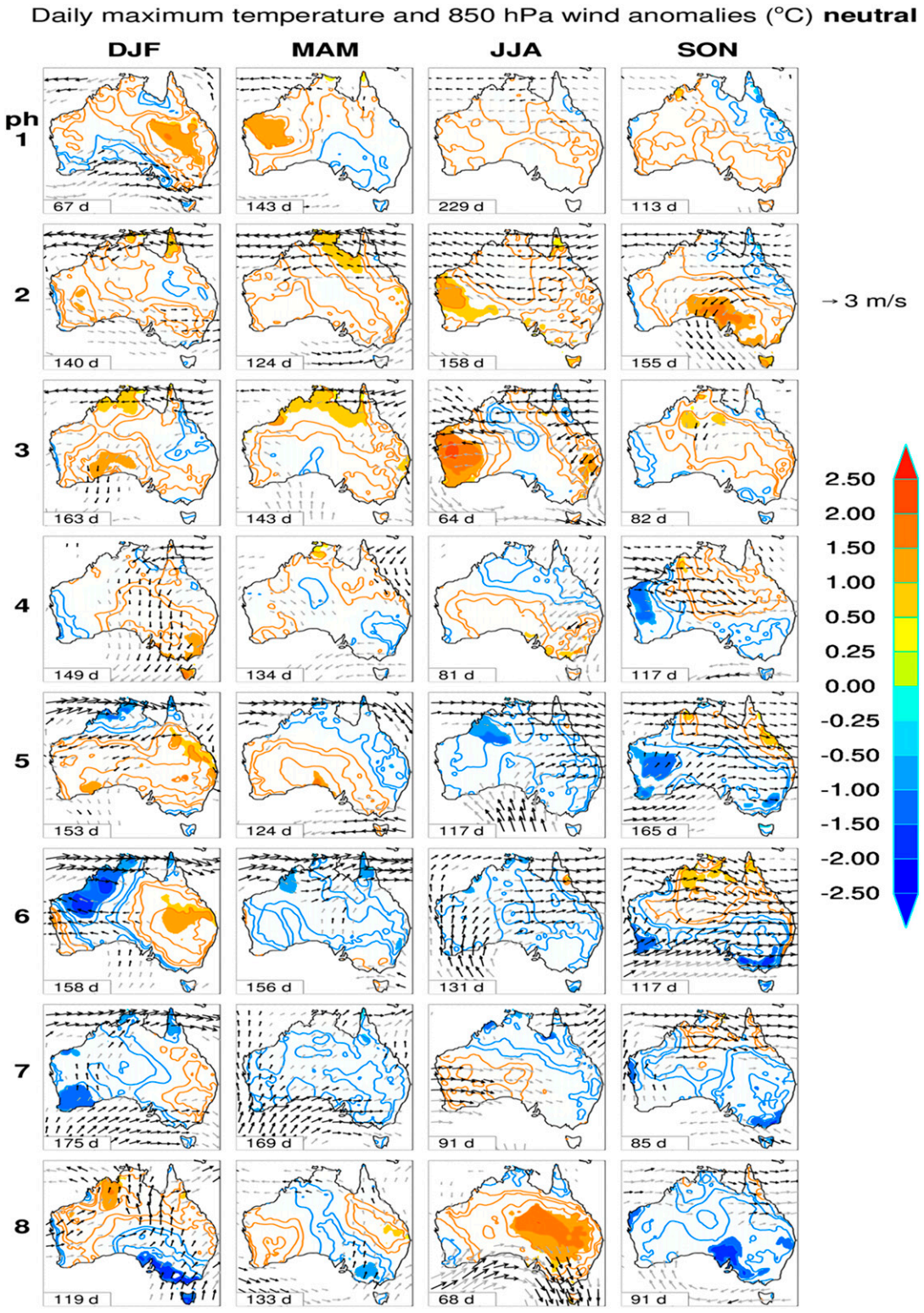

FIG. 12. As in Fig. 1, but for daily maximum temperature during neutral ENSO years.

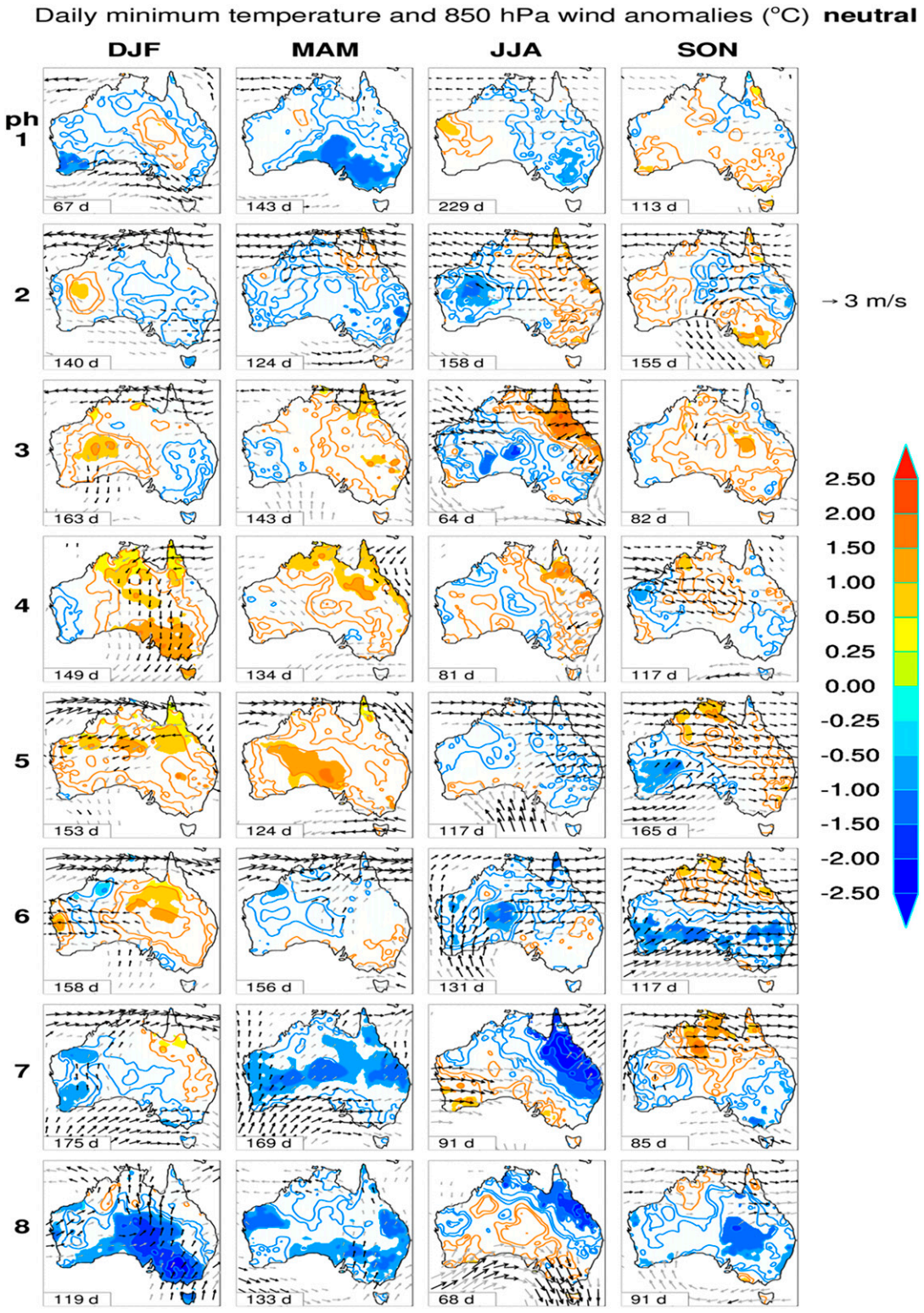

FIG. 13. As in Fig. 1, but for daily minimum temperature during neutral ENSO years.

that top decile daytime heat events are around twice as likely to occur than normal over Victoria and Tasmania when the MJO is in phase 3 in spring (far right column of Fig. 6). When we repeat the analysis for El Niño years only, this increases to more than 3 times the normal likelihood (not shown). These findings are consistent with the typical impact of El Niño in producing warmer than average days and nights in Australia's southeast during spring (Bureau of Meteorology 2022). Conversely, La Niña typically produces cooler than average days in the southeast during spring (Bureau of Meteorology 2022)—this influence is apparent in the 2°C cooling that occurs over southeastern Australia (in conjunction with cyclonic anomalies) when the MJO is in phase 6 during La Niña years (Fig. 10), compared to the 1°C cooling that occurs during neutral ENSO years (Fig. 12). We also note the asymmetry in the magnitude of the MJO's springtime impacts on temperature during El Niño compared to La Niña. For example, the signals during El Niño in MJO phases 3 and 7 for maximum and minimum temperature (Figs. 8 and 9, respectively) are notably stronger than those during La Niña (cf. Figs. 10 and 11, respectively). This is consistent with the impact of asymmetry on rainfall probabilities by El Niño compared to La Niña, which is greatest in spring (Cowan et al. 2022b).

6. Summary and conclusions

In this study we have provided the first comprehensive analysis of the MJO's impact on maximum and minimum temperature and extremes over Australia. We have shown the MJO to have a significant influence on Australian temperatures in all parts of the country at various times throughout the year, and to varying degrees. These influences occur directly in response to the MJO's convective anomalies over northern Australia, primarily during summer, and indirectly in response to remotely forced anomalies in the low-level wind flow over Australia, primarily associated with MJO-induced tropical–extratropical Rossby wave train propagation (Wheeler et al. 2009).

We have also explored the role of ENSO in modulating the MJO's impacts on maximum and minimum temperature. In general, we see changes to the MJO–temperature signals that are consistent with the typical temperature responses to ENSO itself. Daytime temperature anomalies tend to increase during El Niño years and decrease during La Niña years, except over parts of northern Australia in the latter half of the year when these relationships reverse. ENSO's impact on minimum temperature shows a more complex spatial and temporal variation throughout the year, which is again reflected in the changes to the MJO–temperature signal during El Niño and La Niña years. These changes, which are again well explained by anomalies in the circulation, lead to some very strong ENSO-related warming and cooling patterns over parts of the country that appear stronger than the impacts of the MJO alone. This includes daytime warming over central-northern Australia (El Niño) and cooling over most of Australia (La Niña) of up to 2°C in phase 5 during autumn, and overnight cooling (El Niño) and warming (La Niña) of more than 1.5°C over parts of northern Australia in phase 2 during winter.

One of the most pronounced impacts of the MJO on maximum temperature occurs across the southeastern quadrant of Australia in phase 3 during spring, when we see an increase in daytime temperature of up to 1.8°C and a doubling of the normal likelihood of extreme heat, in association with a strong anticyclonic anomaly. As a remote response to enhanced MJO convection over the eastern Indian Ocean, this extratropical anticyclone produces anomalously dry conditions in Victoria, Tasmania, and southeastern South Australia due to large-scale subsidence existing within the anticyclone (Wheeler et al. 2009; Cowan et al. 2022b). While the dry signal is mostly confined to the far southeast, the anomalous warming expands across much of southern Australia under the influence of warm continental northeasterly airflow from the extratropical anticyclone. During El Niño years, when the southern two-thirds of Australia experience above average springtime temperatures and southeastern Australia experiences temperatures in the warmest 30% of climatology, the anticyclonic wind speeds in phase 3 increase over the southeast, the daytime warming intensifies across the south, and top decile heat events become more than 3 times as likely to occur than normal in Victoria and Tasmania.

For minimum temperature, the most prominent impact from the MJO occurs over Queensland in phase 7 during winter, when we see overnight temperature anomalies down to −2°C in some places with more than twice the normal likelihood of extremely cold nights. This results from westerly/southwesterly anomalies that transport cool and dry continental air to northeastern Australia, as a remote response to suppressed MJO convection over the eastern Indian Ocean (Wang and Hendon 2020). During La Niña years, when much of northern and eastern Australia experiences overnight wintertime warming, the southwesterly wind flow is reduced in phase 7 and the cool anomalies weaken by about a factor of a half over Queensland. However, during El Niño years, when northern and eastern Australia experience moderate overnight cooling, the MJO teleconnection to Queensland remains strong. In fact, the cold signal in the southeast, including over southern Queensland, strengthens in phase 7 during El Niño, consistent with where the strongest overnight wintertime cooling occurs for a typical El Niño event.

The results of this work demonstrate the importance of understanding the MJO's impacts on temperature for some of the most agriculturally critical regions in Australia, including the southeast's Murray Darling Basin (e.g., during phase 3 in spring) and southeast Queensland on the western slopes of the Great Dividing Range (e.g., during phase 7 in winter). ENSO's role in modulating these impacts also highlights the importance of understanding multiple modes of variability and their compounding influences on weather and climate (Ridder et al. 2020), particularly considering the strong effect that high-impact events such as heatwaves and flash droughts can have on agricultural productivity across Australia (Nguyen et al. 2019). Future research could thus expand on the work presented here to assess the roles of other key drivers of Australian temperature variability and extremes occurring in combination

with the MJO, including the Indian Ocean dipole, the Southern Annular Mode, and atmospheric blocking (e.g., Marshall et al. 2014). Follow-on work could also use the ocean-based Niño indices to assess the comparative roles of western central Pacific versus eastern Pacific El Niño events (e.g., Larkin and Harrison 2005; Freund et al. 2021) and La Niña events (Marshall et al. 2015; Feng et al. 2021) in modulating the MJO's impacts on temperature. Improved knowledge of these key modes, their interactions, and impacts underpins our ability to improve their depiction and prediction in dynamical forecast systems (e.g., Marshall and Hendon 2019; Marshall et al. 2021), and their teleconnections to agriculture (Anderson et al. 2020), on subseasonal time scales.

Acknowledgments. This work is funded by Meat and Livestock Australia, the Queensland Government through the Drought and Climate Adaptation Program, and the University of Southern Queensland through the Northern Australia Climate Program (NACP). We extend our gratitude to the NACP Climate Mates for providing the motivation for us to undertake this research. We thank Ghyslaine Boschat, Acacia Pepler, and three anonymous reviewers for generously giving their time to help improve the overall quality of this paper. This research was undertaken with the assistance of resources from the National Computational Infrastructure Australia, a National Collaborative Research Infrastructure Strategy enabled capability supported by the Australian Government.

Data availability statement. All observational and reanalysis data are publicly available. AGCD version 1 is available from https://doi.org/10.4227/166/5a8647d1c23e0. The MJO index data can be downloaded from http://www.bom.gov.au/climate/mjo/. Daily wind data from NCEP–NCAR Reanalysis 1 are available at https://psl.noaa.gov/data/gridded/data.ncep.reanalysis.surface.html. The MSLP datasets for Darwin and Tahiti used for calculating the SOI are available from the Bureau of Meteorology via ftp at ftp://ftp.bom.gov.au/anon/home/ncc/www/sco/soi. The Tahiti MSLP data are kindly provided by Météo France interregional direction for French Polynesia. The data in this study were analyzed and plotted using IDL 8.6.0.

REFERENCES

Alexander, L. V., P. Uotila, and N. Nicholls, 2009: Influence of sea surface temperature variability on global temperature and precipitation extremes. *J. Geophys. Res.*, **114**, D18116, https://doi.org/10.1029/2009JD012301.

Anderson, W., Á. G. Muñoz, L. Goddard, W. Baethgen, and X. Chourio, 2020: MJO teleconnections to crop growing seasons. *Climate Dyn.*, **54**, 2203–2219, https://doi.org/10.1007/s00382-019-05109-0.

Arblaster, J. M., and L. V. Alexander, 2012: The impact of the El Niño southern oscillation on maximum temperature extremes. *Geophys. Res. Lett.*, **39**, L20702, https://doi.org/10.1029/2012GL053409.

Bureau of Meteorology, 2022: Climate Driver Update: Climate drivers in the Pacific, Indian and Southern Oceans and the tropics. Bureau of Meteorology, http://www.bom.gov.au/climate/enso/#tabs=Pacific-Ocean&pacific=History.

Camargo, S. J., M. C. Wheeler, and A. H. Sobel, 2009: Diagnosis of the MJO modulation of tropical cyclogenesis using an empirical index. *J. Atmos. Sci.*, **66**, 3061–3074, https://doi.org/10.1175/2009JAS3101.1.

Camp, J., and Coauthors, 2018: Skilful multi-week tropical cyclone prediction in ACCESS-S1 and the role of the MJO. *Quart. J. Roy. Meteor. Soc.*, **144**, 1337–1351, https://doi.org/10.1002/qj.3260.

Cowan, T., and Coauthors, 2019: Forecasting the extreme rainfall, low temperatures, and strong winds associated with the northern Queensland floods of February 2019. *Wea. Climate Extremes*, **26**, 100232, https://doi.org/10.1016/j.wace.2019.100232.

——, M. C. Wheeler, C. de Burgh-Day, H. Nguyen, and D. Cobon, 2022a: Multi-week prediction of livestock chill conditions associated with the northwest Queensland floods of February 2019. *Sci. Rep.*, **12**, 5907, https://doi.org/10.1038/s41598-022-09666-z.

——, ——, and A. G. Marshall, 2022b: The combined influence of the Madden–Julian oscillation and El Niño–Southern Oscillation on Australian rainfall. *J. Climate*, **36**, 313–334, https://doi.org/10.1175/JCLI-D-22-0357.1.

Daley, R., 1993: *Atmospheric Data Analysis*. Cambridge University Press, 472 pp.

Donald, A., H. Meinke, and B. Power, 2006: Near-global impact of the Madden–Julian Oscillation on rainfall. *Geophys. Res. Lett.*, **33**, L09704, https://doi.org/10.1029/2005GL025155.

Evans, A., D. Jones, R. Smalley, and S. Lellyett, 2020: An enhanced gridded rainfall dataset scheme for Australia. Bureau Research Rep. 41, 45 pp.

Feng, M., Y. Zhang, H. Hendon, M. J. McPhaden, and A. G. Marshall, 2021: Niño 4 West (Niño-4W) sea surface temperature variability. *J. Geophys. Res. Oceans*, **126**, e2021JC017591, https://doi.org/10.1029/2021JC017591.

Freund, M. B., A. G. Marshall, M. C. Wheeler, and J. N. Brown, 2021: Central Pacific El Niño as a precursor to summer drought-breaking rainfall over southeastern Australia. *Geophys. Res. Lett.*, **48**, e2020GL091131, https://doi.org/10.1029/2020GL091131.

Ghelani, R. P. S., E. C. J. Oliver, N. J. Holbrook, M. C. Wheeler, and P. J. Klotzbach, 2017: Joint modulation of intraseasonal rainfall in tropical Australia by the Madden–Julian Oscillation and El Niño–Southern Oscillation. *Geophys. Res. Lett.*, **44**, 10 754–10 761, https://doi.org/10.1002/2017GL075452.

Gill, A. E., 1980: Some simple solutions for heat-induced tropical circulation. *Quart. J. Roy. Meteor. Soc.*, **106**, 447–462, https://doi.org/10.1002/qj.49710644905.

Glowacki, T. J., Y. Xiao, and P. Steinle, 2012: Mesoscale surface analysis system for the Australian domain: Design issues, development status, and system validation. *Wea. Forecasting*, **27**, 141–157, https://doi.org/10.1175/WAF-D-10-05063.1.

Hendon, H. H., and B. Liebmann, 1990: The intraseasonal (30–50 day) oscillation of the Australian summer monsoon. *J. Atmos. Sci.*, **47**, 2909–2924, https://doi.org/10.1175/1520-0469(1990)047<2909:TIDOOT>2.0.CO;2.

——, C. Zhang, and J. D. Glick, 1999: Interannual variation of the Madden–Julian oscillation during austral summer. *J. Climate*, **12**, 2538–2550, https://doi.org/10.1175/1520-0442(1999)012<2538:IVOTMJ>2.0.CO;2.

Jones, D. A., W. Wang, and R. Fawcett, 2009: High-quality spatial climate data-sets for Australia. *Aust. Meteor. Oceanogr. J.*, **58**, 233–248, https://doi.org/10.22499/2.5804.003.

Kalnay, E., and Coauthors, 1996: The NCEP/NCAR 40-Year Reanalysis Project. *Bull. Amer. Meteor. Soc.*, **77**, 437–471, https://doi.org/10.1175/1520-0477(1996)077<0437:TNYRP>2.0.CO;2.

Kiladis, G. N., J. Dias, K. H. Straub, M. C. Wheeler, S. N. Tulich, K. Kikuchi, K. M. Weickmann, and M. J. Ventrice, 2014: A comparison of OLR and circulation-based indices for tracking the MJO. *Mon. Wea. Rev.*, **142**, 1697–1715, https://doi.org/10.1175/MWR-D-13-00301.1.

Klotzbach, P. J., 2014: The Madden–Julian oscillation's impacts on worldwide tropical cyclone activity. *J. Climate*, **27**, 2317–2330, https://doi.org/10.1175/JCLI-D-13-00483.1.

Larkin, N., and D. E. Harrison, 2005: On the definition of El Niño and associated seasonal average U.S. weather anomalies. *Geophys. Res. Lett.*, **32**, L13705, https://doi.org/10.1029/2005GL022738.

Lau, K.-M., L. Peng, C. H. Sui, and T. Nakazawa, 1989: Dynamics of super cloud clusters, westerly wind bursts, 30–60 day oscillations and ENSO: A unified view. *J. Meteor. Soc. Japan*, **67**, 205–219, https://doi.org/10.2151/jmsj1965.67.2_205.

Lee, R. W., S. J. Woolnough, A. J. Charlton-Perez, and F. Vitart, 2019: ENSO modulation of MJO teleconnections to the North Atlantic and Europe. *Geophys. Res. Lett.*, **46**, 13 535–13 545, https://doi.org/10.1029/2019GL084683.

Leroy, A., and M. C. Wheeler, 2008: Statistical prediction of weekly tropical cyclone activity in the Southern Hemisphere. *Mon. Wea. Rev.*, **136**, 3637–3654, https://doi.org/10.1175/2008MWR2426.1.

Liebmann, B., H. Hendon, and J. D. Glick, 1994: The relationship between tropical cyclones of the western Pacific and Indian Oceans and the Madden–Julian oscillation. *J. Meteor. Soc. Japan*, **72**, 401–412, https://doi.org/10.2151/jmsj1965.72.3_401.

Lim, E.-P., and Coauthors, 2021: Why Australia was not wet during spring 2020 despite La Niña. *Sci. Rep.*, **11**, 18423, https://doi.org/10.1038/s41598-021-97690-w.

Madden, R. A., and P. R. Julian, 1971: Detection of a 40–50 day oscillation in the zonal wind in the tropical Pacific. *J. Atmos. Sci.*, **28**, 702–708, https://doi.org/10.1175/1520-0469(1971)028<0702:DOADOI>2.0.CO;2.

——, and ——, 1972: Description of global-scale circulation cells in the tropics with a 40–50 day period. *J. Atmos. Sci.*, **29**, 1109–1123, https://doi.org/10.1175/1520-0469(1972)029<1109:DOGSCC>2.0.CO;2.

Marshall, A. G., and H. H. Hendon, 2019: Multi-week prediction of the Madden–Julian oscillation with ACCESS-S1. *Climate Dyn.*, **52**, 2513–2528, https://doi.org/10.1007/s00382-018-4272-6.

——, D. Hudson, M. C. Wheeler, O. Alves, H. H. Hendon, M. J. Pook, and J. S. Risbey, 2014: Intra-seasonal drivers of extreme heat over Australia in observations and POAMA-2. *Climate Dyn.*, **43**, 1915–1937, https://doi.org/10.1007/s00382-013-2016-1.

——, H. H. Hendon, M. Feng, and A. Schiller, 2015: Initiation and amplification of the Ningaloo Niño. *Climate Dyn.*, **45**, 2367–2385, https://doi.org/10.1007/s00382-015-2477-5.

——, ——, and D. Hudson, 2016: Visualizing and verifying probabilistic forecasts of the Madden–Julian Oscillation. *Geophys. Res. Lett.*, **43**, 12 278–12 286, https://doi.org/10.1002/2016GL071423.

——, ——, and ——, 2021: Influence of the Madden–Julian Oscillation on multiweek prediction of Australian rainfall extremes using the ACCESS-S1 prediction system. *J. South. Hemisphere Earth Syst. Sci.*, **71**, 159–180, https://doi.org/10.1071/ES21001.

——, G. Wang, H. H. Hendon, and H. Lin, 2022: Madden–Julian Oscillation teleconnections to Australian springtime temperature extremes and their prediction in ACCESS-S1. *Climate Dyn.*, https://doi.org/10.1007/s00382-022-06586-6, in press.

Matthews, A. J., 2000: Propagation mechanisms for the Madden–Julian Oscillation. *Quart. J. Roy. Meteor. Soc.*, **126**, 2637–2652, https://doi.org/10.1002/qj.49712656902.

McBride, J. L., and N. Nicholls, 1983: Seasonal relationships between Australian rainfall and the Southern Oscillation. *Mon. Wea. Rev.*, **111**, 1998–2004, https://doi.org/10.1175/1520-0493(1983)111<1998:SRBARA>2.0.CO;2.

Min, S.-K., W. Cai, and P. Whetton, 2013: Influence of climate variability on seasonal extremes over Australia. *J. Geophys. Res. Atmos.*, **118**, 643–654, https://doi.org/10.1002/jgrd.50164.

Moon, J.-Y., B. Wang, and K.-J. Ha, 2011: ENSO regulation of MJO teleconnection. *Climate Dyn.*, **37**, 1133–1149, https://doi.org/10.1007/s00382-010-0902-3.

Nguyen, H., M. C. Wheeler, J. A. Otkin, T. Cowan, A. Frost, and R. Stone, 2019: Using the evaporative stress index to monitor flash drought in Australia. *Environ. Res. Lett.*, **14**, 064016, https://doi.org/10.1088/1748-9326/ab2103.

Nix, H. A., 1987: The Australian climate and its effects on grain yield and quality. *Australian Field Crops, Wheat and Other Temperate Cereals*, Vol. 1, A. Lazenby A and E. M. Matheson, Eds., Angus and Robertson, 570 pp.

Pook, M. J., P. C. McIntosh, and G. A. Meyers, 2006: The synoptic decomposition of cool-season rainfall in the southeastern Australian cropping region. *J. Appl. Meteor. Climatol.*, **45**, 1156–1170, https://doi.org/10.1175/JAM2394.1.

——, S. Lisson, J. Risbey, C. C. Ummenhofer, P. McIntosh, and M. Rebbeck, 2009: The autumn break for cropping in southeast Australia: Trends, synoptic influences and impacts on yield. *Int. J. Climatol.*, **29**, 2012–2026, https://doi.org/10.1002/joc.1833.

Ramsay, H. A., S. J. Camargo, and D. Kim, 2012: Cluster analysis of tropical cyclone tracks in the Southern Hemisphere. *Climate Dyn.*, **39**, 897–917, https://doi.org/10.1007/s00382-011-1225-8.

Ridder, N., and Coauthors, 2020: Global hotspots for the occurrence of compound events. *Nat. Commun.*, **11**, 5956, https://doi.org/10.1038/s41467-020-19639-3.

Roundy, P. E., K. MacRitchie, J. Asuma, and T. Melino, 2010: Modulation of the global atmospheric circulation by combined activity in the Madden–Julian oscillation and the El Niño–Southern Oscillation during boreal winter. *J. Climate*, **23**, 4045–4059, https://doi.org/10.1175/2010JCLI3446.1.

Son, S.-W., Y. Lim, C. Yoo, H. H. Hendon, and J. Kim, 2017: Stratospheric control of the Madden–Julian oscillation. *J. Climate*, **30**, 1909–1922, https://doi.org/10.1175/JCLI-D-16-0620.1.

Spiegel, M. R., 1961: *Schaum's Outline of Theory and Problems of Statistics*. McGraw-Hill, 504 pp.

Stone, R., and A. Auliciems, 1992: SOI phase relationships with rainfall in eastern Australia. *Int. J. Climatol.*, **12**, 625–636, https://doi.org/10.1002/joc.3370120608.

——, G. L. Hammer, and T. Marcussen, 1996: Prediction of global rainfall probabilities using phases of the Southern Oscillation Index. *Nature*, **384**, 252–255, https://doi.org/10.1038/384252a0.

Student, 1908: The probable error of a mean. *Biometrika*, **6** (1), 1–25, https://doi.org/10.2307/2331554.

Troup, A. J., 1965: The 'southern oscillation'. *Quart. J. Roy. Meteor. Soc.*, **91**, 490–506, https://doi.org/10.1002/qj.49709139009.

Wang, B., and H. Rui, 1990: Synoptic climatology of transient tropical intraseasonal convection anomalies: 1975–1985. *Meteor. Atmos. Phys.*, **44**, 43–61, https://doi.org/10.1007/BF01026810.

Wang, G., and H. H. Hendon, 2020: Impacts of the Madden–Julian Oscillation on wintertime Australian minimum temperatures and Southern Hemisphere circulation. *Climate Dyn.*, **55**, 3087–3099, https://doi.org/10.1007/s00382-020-05432-x.

Wang, S., D. Ma, A. H. Sobel, and M. K. Tippett, 2018: Propagation characteristics of BSISO indices. *Geophys. Res. Lett.*, **45**, 9934–9943, https://doi.org/10.1029/2018GL078321.

Webb, L., 2013: Impacts on agriculture. *Proc. Roy. Soc. Vic.*, **125**, 24–30, https://doi.org/10.1071/RS13012.

Wheeler, M. C., and H. H. Hendon, 2004: An all-season real-time multivariate MJO index: Development of an index for monitoring and prediction. *Mon. Wea. Rev.*, **132**, 1917–1932, https://doi.org/10.1175/1520-0493(2004)132<1917:AARMMI>2.0.CO;2.

——, and J. L. McBride, 2012: Australasian monsoon. *Intraseasonal Variability in the Atmosphere–Ocean Climate System*, W. K. M. Lau and D. E. Waliser, Eds., 2nd ed. Springer, 147–198, https://doi.org/10.1007/978-3-642-13914-7_5.

——, H. H. Hendon, S. Cleland, H. Meinke, and A. Donald, 2009: Impacts of the Madden–Julian oscillation on Australian rainfall and circulation. *J. Climate*, **22**, 1482–1498, https://doi.org/10.1175/2008JCLI2595.1.

Yamagata, T., and Y. Hayashi, 1984: A simple diagnostic model for the 30–50 day oscillation in the tropics. *J. Meteor. Soc. Japan*, **62**, 709–717, https://doi.org/10.2151/jmsj1965.62.5_709.